Initial Validation of a Gas-Granular Flow Solver Using a Subscale, Reduced Pressure Plume Surface Interaction Ground Test

Jeffrey S. West[1] and Jason Howison[2]
NASA Marshall Space Flight Center, Huntsville, AL, 35808, USA

Peter Liever[3], Timothy Dawson[4], Thomas Shurtz[5], and Andrew Weaver[6]
Jacobs Space Exploration Group, NASA Marshall Space Flight Center, Huntsville, AL, 35808, USA

With NASA's goal to land the next humans on the lunar surface in the next few years, it is vitally important to have a better understanding of the plume surface interaction (PSI) between the landing vehicles and the lunar regolith. The Fluid Dynamics Branch at NASA/MSFC has previously used the gas-granular flow solver Loci/GGFS to qualitatively predict crater formation due to PSI effects in a lunar (near vacuum) ambient environment. In this paper, validation of Loci/GGFS crater width and depth predictions in ambient near-lunar conditions are provided using experimental data collected at MSFC during the Physics-Focused Ground Test 1 (PFGT-1) campaign in 2022. To observe sensitivity to soil models, simulations were conducted with both monodisperse glass bead (MGB) and BP-1 lunar regolith simulant soil models in Loci/GGFS. Crater depth and width comparisons are made with PFGT-1 Run 56, which used BP-1 soil. The Loci/GGFS BP-1 soil model performed slightly better with a mean predicted crater depth within 10% of the experiment. Both soil models predicted crater width within 10%. Cratering occurred more quickly with the MGB soil model. Mesh and spatial order sensitivity are also examined for the BP-1 soil model.

I. Nomenclature

D	diameter
$e_{g,o}$	internal energy
g	gravity vector
h	nozzle height, enthalpy
I	interphase momentum transfer
J	fluctuating velocity/force correlation
p	pressure
q	conductive heat flux
$\mathbf{R_u}$	pseudo-turbulent Reynolds stress
$\mathbf{u}$	velocity
α	volume fraction

[1] AST, MSFC Fluid Dynamics Branch, AIAA Senior Member
[2] Senior Research Engineer, CFD Research Corporation
[3] Technical Fellow, CFD Research Corporation, AIAA Senior Member
[4] Senior Research Engineer, CFD Research Corporation
[5] Fluid Dynamicist, Jacobs
[6] Senior Engineer, Sev1Tech, and AIAA Senior Member

γ	granular dissipation rate
θ	granular temperature
λ	granular bulk viscosity
μ	granular shear viscosity
ρ	density
$\boldsymbol{\tau}$	shear stress tensor

Subscripts

g	gas phase
s	solid phase

II. Introduction

Plume surface interaction (PSI) is a major risk during propulsive descent/ascent on unprepared surfaces. It poses significant risks to the vehicle, nearby assets, and the crew via: 1) plume-induced cratering that can lead to landing on an uneven surface, 2) obscuration of the landing surface due to eroded dust, 3) high-speed ejecta/debris impacts to the vehicle or nearby assets during descent or ascent, and/or 4) impingement of the plume on nearby structures. With human missions planned for the Moon and potentially Mars in the near future, PSI modeling and simulation will be an essential design tool that can help mitigate associated PSI risks.

The Fluid Dynamics Branch in the Propulsion Department (ER42) at NASA Marshall Space Flight Center has developed a cascade of predictive simulation capabilities for PSI at various levels of fidelity to address and mitigate PSI risks to landers and landing missions in a timely manner. This includes the development of the multi-phase, multi-physics Gas Granular Flow Solver (GGFS) simulation tool [1], [2] at the higher-fidelity end of the predictive simulation capability spectrum. GGFS has been implemented in the Loci framework [3]. Loci/GGFS is designed to capture the progression from surface erosion onset to large scale soil bed fluidization and deep cratering expected to occur for high thrust lander PSI such as proposed HLS configurations. Hybrid Computational Fluid Dynamics (CFD)/engineering model tools have also been developed [4]. The hybrid CFD/engineering model approach decreases the turnaround time for metrics such as crater depth through the assumption of viscous shear erosion only and a corresponding viscous shear erosion model anchored to Apollo flight data. This cascade of tools allows applications suitable to different risk postures and different times in design and analysis cycles. These predictive simulation models are currently being used for NASA Flight Programs such as the Human Landing System (HLS), Commercial Lunar Payload Services (CLPS), and PSI induced environments affecting Lunar Site Planning.

The gas-granular flow solver Loci/GGFS was developed explicitly for modeling plume impingement flow on extraterrestrial soils. Loci/GGFS is a multi-phase flow solver that treats both the gas and granular phases with an Eulerian modeling approach. By treating the solid phase as a continuum that averages the motion of individual particles, it is possible to simulate dense, solid phase flows without very long computation times or memory requirements that would be encountered with a Lagrangian particle treatment; the range of scales challenge is mitigated. An Eulerian granular mechanics model is implemented in Loci/GGFS that relies on closure models to describe particle-particle and particle-fluid interactions.

In 2022, the Physics-Focused Ground Test 1 (PFGT-1) was conducted at Marshall Space Flight Center [5]. In these vacuum chamber experiments, a supersonic plume was bisected by a transparent splitter plater before interacting with a bin of prepared granular material. Conducting the experiment in this manner enabled visualization of crater formation throughout the tests. By running the tests in a vacuum chamber, the ambient conditions could be controlled to match near-lunar or Martian conditions. Six different granular soils were used in PFGT-1 including monodisperse glass beads (MGB) and BP-1 lunar regolith simulant. Cratering of different granular materials under the same impingement conditions provides insight on how soil properties can impact crater formation.

In this paper, experimental data from PFGT-1 will be used to begin the process of validation of Loci/GGFS crater depth and width predictions. The experimental case used herein was conducted at near-lunar ambient conditions with a BP-1 soil bed. To examine the effect of soil modeling in Loci/GGFS, both MGB and BP-1 soil models are considered. Mesh and solver spatial order accuracy sensitivity studies will be presented for the BP-1 soil model.

III. Brief History of PSI Computational Model Development

In the post-Apollo era, groundbreaking work towards characterizing and predicting the effects of lander rocket plume surface interaction induced surface erosion and cratering environments was performed by Dr. Philip Metzger at the NASA/KSC Granular Mechanics and Regolith Operations (GMRO) laboratory, aka SwampWorks, in the early

2000s [6]-[9]. Metzger performed fundamental experiments of jet impingement on sand and regolith simulant beds, reduced gravity flight PSI experiments, and unit physics experiments to characterize regolith properties such as porosity and cohesion. He formulated the extraordinary physics modeling challenges of extraterrestrial flow of regolith granular materials that feature irregular-shaped particles with jagged interlocking surface features and occur in polydisperse soil mixtures that result in high cohesion and low porosity.

Metzger pursued development of gas-particle interaction modeling for the relevant erosion mechanisms of viscous erosion (VE), diffusion-driven shearing (DDS), bearing capacity failure (BCF), and diffused gas eruption (DGE). The complexities of gas-granular two-phase flow interaction required collaborative model development from the granular flow modeling and the multi-physics computational fluid dynamics modeling communities. He established cooperation with chemical engineering academic partners who offered a wealth of expertise in complex granular material flow modeling, notably Prof. J. Curtis at the University of Florida (now University of California at Davis) and Prof. C. Hrenya (University of Colorado). Collaboration focused on model formulations for lunar regolith driven by the complexity of jagged, interlocking particle shapes and broad particle size mixtures. The Curtis group development resulted in a granular material constituent model and closure models for stress, drag, conduction, and dissipation of granular kinetics of non-spherically shaped particles for implementation in granular flow CFD models [10]. The Hrenya group extended mono-disperse granular kinetic theory to poly-disperse mixture formulations for discrete numbers of size bins [11]-[14]. These developments resulted in granular phase constitutive models ready for implementation in an Eulerian-Eulerian two-fluid CFD framework.

Metzger initiated collaboration between the academic model developers and multi-phase, multi-physics computational tool developers at CFD Research Corporation to develop a computational framework capable of modeling plume induced erosion modeling for rocket plumes in a lunar vacuum environment. This development was sponsored through multiple NASA SBIR/STTR grants from 2008 through 2012 and resulted in the Gas-Granular Flow Solver (GGFS) [1], [2]. NASA adopted the GGFS framework in the 2016 timeframe for lunar and Mars lander project analysis support and sponsored migration to the highly parallelized Loci framework for execution on NASA/ARC high performance computing assets. The resulting Loci/GGFS framework today constitutes the most advanced PSI predictive analysis tool available to the NASA community and the only one to date capable of modeling polydisperse irregular particle mixture effects.

IV. Loci/GGFS Flow Solver

The governing equations of the Loci/GGFS flow solver and basic numerical approach are now discussed. More details on the flow solver are available in the literature [1], [2], [15], [16]. The compressible Eulerian-Eulerian flow solver is based on the governing equations of continuity,

$$\frac{\partial}{\partial t}\left(\alpha_g\rho_g\right) + \boldsymbol{\nabla}\cdot\left(\alpha_g\rho_g\mathbf{u_g}\right) = 0 \tag{1}$$

$$\frac{\partial}{\partial t}\left(\alpha_s\rho_s\right) + \boldsymbol{\nabla}\cdot\left(\alpha_s\rho_s\mathbf{u_s}\right) = 0 \tag{2}$$

momentum,

$$\frac{\partial}{\partial t}\left(\alpha_g\rho_g\mathbf{u_g}\right) + \boldsymbol{\nabla}\cdot\left(\alpha_g\rho_g\mathbf{u_g}\otimes\mathbf{u_g}\right) = -\boldsymbol{\nabla}\cdot\left(\alpha_g\mathbf{R_u}\right) - \alpha_g\nabla p_g + \boldsymbol{\nabla}\cdot\boldsymbol{\tau}_\mathbf{g} + \alpha_g\rho_g\mathbf{g} + \mathbf{I}_{\mathbf{s-g}}^{\mathbf{mom}} \tag{3}$$

$$\begin{aligned}\frac{\partial}{\partial t}\left(\alpha_s\rho_s\mathbf{u_s}\right) &+ \boldsymbol{\nabla}\cdot\left[\alpha_s\left(\rho_s\mathbf{u_s}\otimes\mathbf{u_s} + p_g\mathbf{I}\right) + p_s\mathbf{I}\right] \\ &= \nabla\cdot\left(\boldsymbol{\tau}_\mathbf{s} + \frac{\alpha_s}{\alpha_g}\boldsymbol{\tau}_\mathbf{g}\right) + \left(p_g\mathbf{I} - \frac{1}{\alpha_g}\boldsymbol{\tau}_\mathbf{g}\right)\nabla\alpha_s + \alpha_s\rho_s\mathbf{g} - \mathbf{I}_{\mathbf{s-g}}^{\mathbf{mom}}\end{aligned} \tag{4}$$

and energy,

$$\frac{\partial}{\partial t}(\alpha_g\rho_g e_{g,o}) + \boldsymbol{\nabla}\cdot\left(\alpha_g(\rho_g e_{g,o} + p_g)\right) = -\boldsymbol{\nabla}\cdot(\alpha_g\mathbf{u_g}\cdot\mathbf{R_u}) + \boldsymbol{\nabla}\cdot(\mathbf{u_g}\cdot\boldsymbol{\tau}_\mathbf{g}) + \boldsymbol{\nabla}\cdot\mathbf{q_g} + \sum_{k=1}^{N_g}(\nabla\cdot\rho hV)_{g,k} + \mathbf{I_{s-g}^{mom}}\cdot\mathbf{u_g} + I_{s-g}^{energy} \tag{5}$$

$$\frac{\partial}{\partial t}(\alpha_s\rho_s e_{s,o}) + \boldsymbol{\nabla}\cdot\left[\left(\alpha_s(\rho_s e_{s,o} + p_g) + p_s\right)\mathbf{u_s}\right] = \boldsymbol{\nabla}\cdot\left[\mathbf{u_s}\cdot\left(\boldsymbol{\tau}_\mathbf{s} + \frac{\alpha_s}{\alpha_g}\boldsymbol{\tau}_\mathbf{g}\right)\right] + \alpha_s\rho_s\mathbf{g}\cdot\mathbf{u_s} + \left(p_g\mathbf{I} - \frac{1}{\alpha_g}\boldsymbol{\tau}_\mathbf{g}\right) - \mathbf{I_{s-g}^{mom}}\cdot\mathbf{u}_s + \boldsymbol{\nabla}\cdot\mathbf{q}_s - I_{s-g}^{energy} \tag{6}$$

for gas-solid and multi-phase interactions. A transport equation is also required for the granular temperature of the mixture,

$$\frac{3}{2}\left[\frac{\partial}{\partial t}(\alpha_s\rho_s\theta) + \boldsymbol{\nabla}\cdot(\alpha_s\rho_s\mathbf{u_s}\theta)\right] = \boldsymbol{\nabla}\cdot\lambda\nabla\theta + \mathbf{P_s}:\boldsymbol{\nabla}\mathbf{u_s} - J_s - \gamma_s \tag{7}$$

The particle-fluid interactions may be represented by drag models that allow momentum exchange between the phases. The particle-particle interactions that govern kinetic theory are the solid stresses, collisional dissipation rate, and solid conductivity. The solid conductivity is currently neglected in Loci/GGFS since the granular conductivity is not significant for the moderately dense and dense particle flows encountered in cratering. It may be included in the future as it may impact representation of dust clouds. The solid phase stress terms appearing in Eqs. (4) and (7) are modeled using constitutive relations based on kinetic theory in the case of spherical particles [17] or using unit physics Discrete Element Method (DEM) simulations over the range of particle shapes, mixture species fractions, and packing densities for non-spherical particles [18], [19], [20].

V. Soil Modeling

Realistic lunar surface bed particle compositions are neither simply spherical nor monodisperse. The lunar regolith, as the extreme example, is poorly sorted with broad particle size distributions and large fines content resulting in low porosity of the soil and resistance to soil fluidization. It has significant cohesion due to interlocking particle shapes from the very jagged particles. The combination of particle shape and size distribution has been identified as major drivers in the complex particle flow response and resulting crater shape characteristics of extraterrestrial granular material. The effects of the wide range of regolith mixture particle sizes, particularly the presence of the small particle sizes, result in increased particle-particle interaction effects and low porosity of the regolith mixture bed.

While particle phase flow closure models for spherical particles can be formulated from particle kinetic theory, closure models for realistic non-spherical particles must be extracted from unit physics DEM particle interaction simulations and provided in the form of tabular datasets. The effects of irregular particle shape can be simulated by approximating the particle features (non-spherical shape factors, angular particle surface roughness, and interlocking features) in the form of multisphere particles - grouped elemental spheres to form composite particles - in the DEM simulations [10], [21]. The LIGGGHTS DEM solver framework serves as the basis for an automated scripted database generation process that determines the required shear flow interparticle kinetic and collisional stresses and energy dissipation properties and packages them into a dataset that is loaded into a GGFS simulation for interpolation during runtime execution [22].

Loci/GGFS thus is equipped to simulate the complete range of modeling approaches: monodisperse spherical particles, polydisperse spherical particle mixtures, monodisperse irregularly-shaped particles, and polydisperse irregularly-shaped particle mixtures. Closure models for spherical particle monodisperse and polydisperse mixtures can be derived from kinetic energy formulations in combination with a particle mixture model introduced by Garzo, Hrenya & Dufty (GHD) which models the polydisperse mixture as a finite set of distinct particle size bins [11]-[14]. The range of particle sizes found in a lunar regolith or simulant mix can be simulated by binning the particle sizes into an appropriate finite number of particle-size species and solving the problem as a multi-species mixture. Assessments during the original GHD mixture model development indicated that a single digit number of particle bins will adequately resolve the properties of lunar regolith soil compositions. Combining these two modeling approaches enables simulations to capture both the contributions of the irregular particle shapes and the particle size distribution.

In this work, spherical monodisperse glass beads (MGB) and monodisperse BP-1 lunar regolith simulant particles are used. To generate a monodisperse BP-1 soil model, a representative BP-1 particle shape and surface topology were obtained from an academic collaborator using Synchrotron Micro-Computed Tomography (SMT) [23]. With this technology, the surface topology of a small number of BP-1 particles sieved to approximately 350 micron size was captured. The outer mold line surface was loaded into the CLUMPS program [24] and the volume shape approximated as a multi-sphere with elemental spheres of varying sizes with user-controlled partial overlap (Fig. 1). Resolutions with 25, 50, and 75 sub-particles were evaluated, as shown in Fig. 2. Assessments concluded that the 50-particle resolution provided adequate resolution, with diminishing benefits for higher resolution. LIGGGHTS DEM simulations were used with the 50-particle resolution multisphere to generate the requisite closure models for the BP-1 soil model.

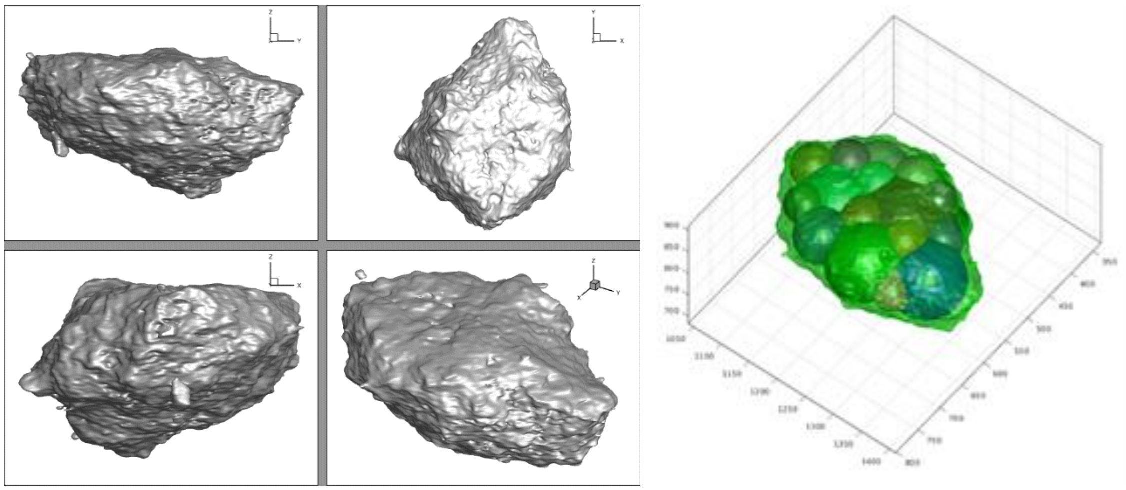

Fig. 1 Left: Particle scan of 350-micron size BP-1 particle. Right: CLUMPS generated multi-sphere resolution embedded within scanned particle outer mold line.

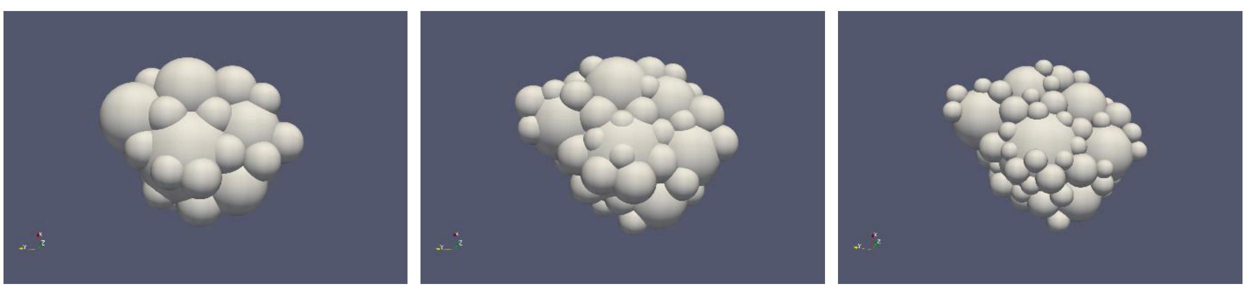

Fig. 2 CLUMPS generated multi-sphere composite particle resolution with 25, 50, 75 elemental spheres (left to right).

VI. Loci/GGFS Validation to Date

Verification of Loci/GGFS was conducted using the Method of Manufactured Solution (MMS) throughout its development. The Method of Manufactured Solutions is an efficient procedure that is widely used in the verification of complex code infrastructures to ensure the model equations are being solved correctly. As new features have been implemented, MMS verification of the new features has been included when appropriate [25].

The most recent validation evidence for Loci/GGFS is that described within the final reporting of the NASA STMD GCD PSI Project (West, J. S., October 2022). In this work, Loci/GGFS was shown to predict crater depth as a function of time to an accuracy range of 4 to 24 percent for three different velocities of subsonic air jets impinging on a bed of monodisperse spherical steel particles[reference this work]. Comparison of the simulation crater depth as a function of time to experimental data is shown in Fig. 3.

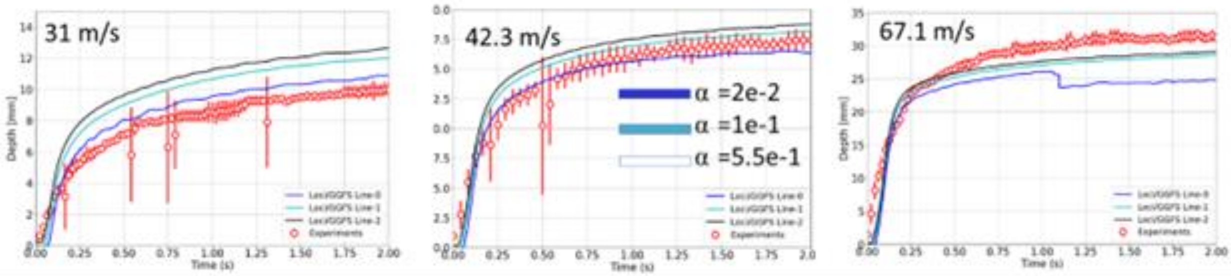

Fig. 3 Comparison of crater depth as a function of time from Loci/GGFS and the data of LaMarche [ref] for three jet velocities.

The pathfinder Loci/GGFS simulation of the PFGT-1 Run 142 was compared to experimental results [26]. The operating conditions for PFGT-1 Run 142 were a nozzle exit plane height to nozzle exit diameter ratio of h/D = 10 with an ambient pressure of 600 Pa and a nozzle mass flow rate of 8.6x10^{-3} kg/s of nitrogen. The soil bed in Run 142 was MGB, and Loci/GGFS used an MGB soil model in this analysis. The degree of agreement between the simulation and experimental results deserved the descriptive term of qualitative validation achievement. Comparison of the simulation crater depth at a time of 1.95 seconds to experimental data is shown in Fig. 4 in which the simulation is within about 22 percent of the experimental results.

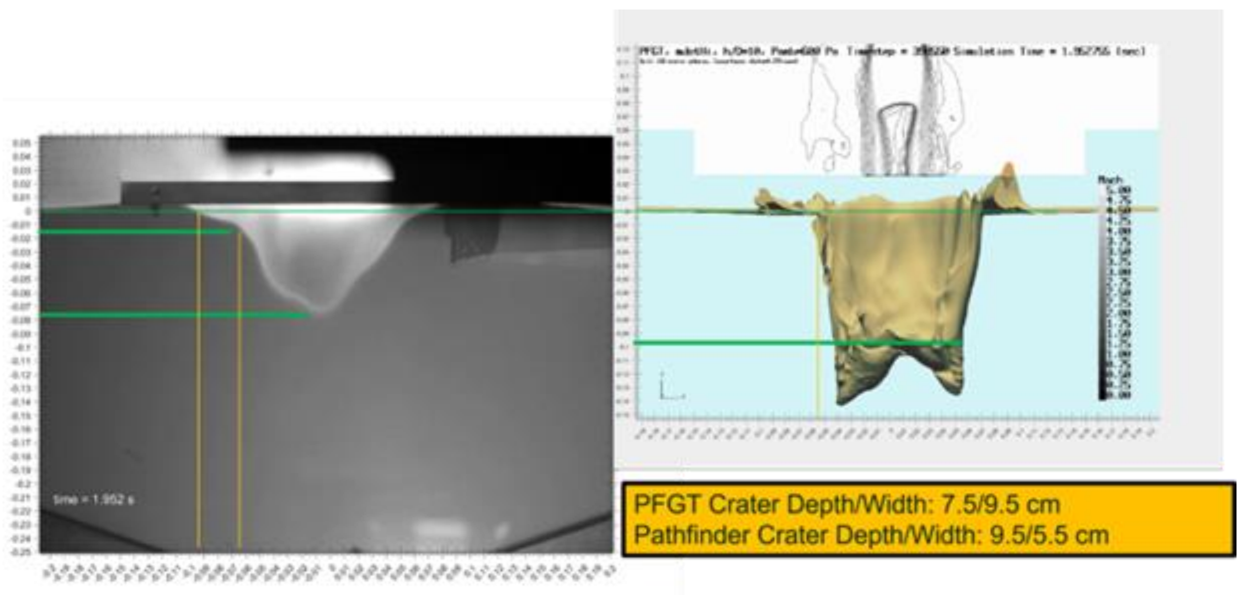

Fig. 4 Comparison of simulated and experimentally-observed crater depth on the splitter plate surface from the Loci/GGFS pathfinder and PFGT-1 Run 142.

The Loci/GGFS validation assessment presented in this paper will use a PFGT-1 case where the soil bed is composed of BP-1 lunar regolith simulant. Cratering predictions were generated using both MGB and monodisperse BP-1 soil models to see how sensitive cratering predictions are to soil models. In planned future Loci/GGFS validation assessments, additional PFGT-1 cases and polydisperse soil models will be explored. This work is already underway.

VII. PFGT-1 Experimental Setup

The geometry of the PFGT-1 experimental setup is described in this section. The test included a nozzle test assembly that was centered above a splitter plate designed to split the nozzle flow in half, such that half of the nozzle flow impinged on the 80 cm x 40 cm x 30 cm soil bin and half flowed outside of the soil bin. A transparent, acrylic viewing pane was used along the splitter plate so that the cratering process could be observed during the test. This experimental setup with dimensions of key components is detailed in References [5] and [27] and is illustrated in Fig. 5.

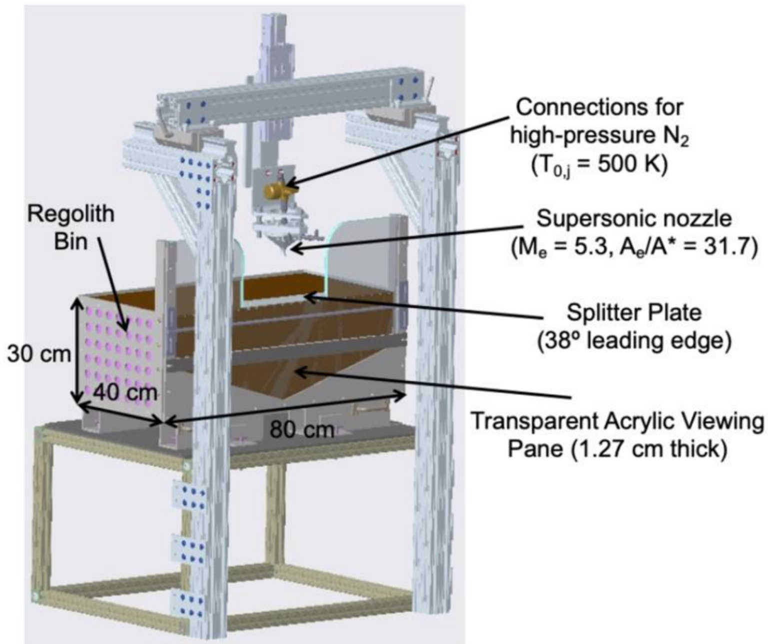

Fig. 5 Cratering test article [27].

The nozzle height settings were set with respect to the nozzle exit plane and the initial regolith surface plane. The target *h*/*D* nozzle heights were achieved by setting the nozzle height relative to the impingement surface based on pre-determined settings from position calibrations of the vertical, linear translating stage. A score line on the viewing pane was used as a reference fill level for the soil simulants. This line was located 2.12 cm below the leading edge of the 1.63 cm tall splitter plate. After filling the soil bin to the target fill level to the best of the test engineers' abilities, target *h*/*D* conditions were then achieved by adjusting vertical position settings to compensate for surface under- or overfills. The locations for the nozzle height, splitter plate height, score line, and actual fill level are illustrated in Fig. 6. This image was taken before PFGT-1 Run 56 (the focus of this work), and it is worth noting the approximately 4 mm variation in initial soil level just from this viewing angle. Directly beneath the nozzle, the initial soil level is 0.46 cm below the bottom edge of the splitter plate (14.3 cm below the nozzle exit plane). The nominal *h*/*D* for PFGT-1 Run 56 was 10, but the actual was 10.33.

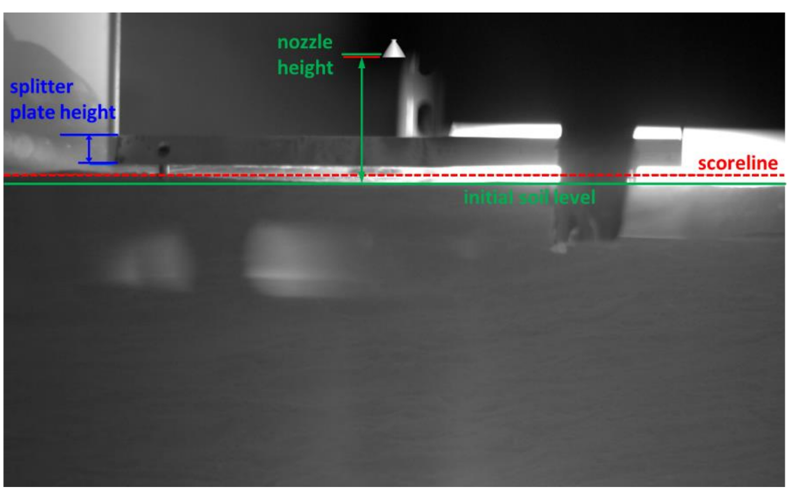

Fig. 6 Illustration of nozzle height, splitter plate, soil bin score line, and soil bin fill level dimensions for PFGT-1 Run 56.

VIII. PFGT-1 Validation Data Selection

For the current Loci/GGFS validation assessment, a PFGT-1 test run using BP-1 soil with clear evidence of diffusion-driven erosion was necessary. In addition, a test with high values of impingement pressure and shear stress on the soil were desired to best match expected engine conditions in upcoming CLPS and HLS missions. Loci/CHEM simulations of plume impingements on a hard surface using PFGT-1 experimental conditions provided expected maximum impingement pressures and shear stresses for each PFGT-1 test condition.

PFGT-1 Run 56 was identified as possessing the maximum impingement pressure and shear stress while simultaneously producing a clearly observable evolution of crater edges on the splitter plate. The nominal operating conditions for PFGT-1 Run 56 were h/D = 10 with an ambient pressure of 267 Pa and a nozzle mass flow rate of 0.32×10^{-3} kg/s. A single frame showing the state of the crater camera at 0.462 seconds after start during PFGT-1 Run 56 is shown in Fig. 7. The flying chunks of soil and ejecta streams provide clear evidence of diffusion-driven erosion.

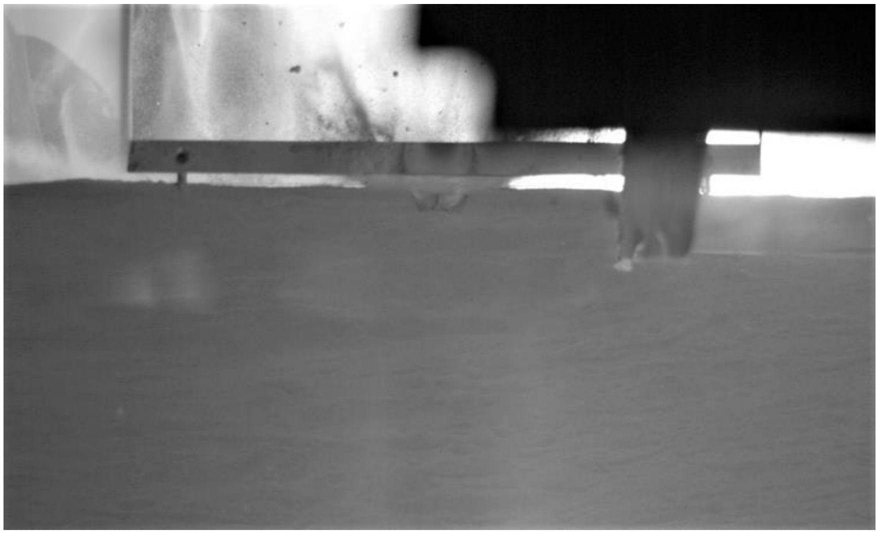

Fig. 7 Single frame of crater camera view at 0.462 seconds after start during the PFGT-1 Run 56 operation.

Maximum crater depth and width were determined manually for the experimental data. Known dimensions on the splitter plate geometry were used to convert pixels into length. Using this calibration, the crater depth and width at the splitter plate were determined at snapshots throughout the experiment. Two authors on this paper both independently determined maximum crater depth using this method. Their results for the first second of the experiment are shown on the left in Fig. 8. Only one author determined maximum crater width at the splitter plate. His results for crater width appear on the right in Fig. 8. No results for the maximum crater depth and width are given for the initial tenths of a second because imagery was obscured by eroded particles during this portion of the run.

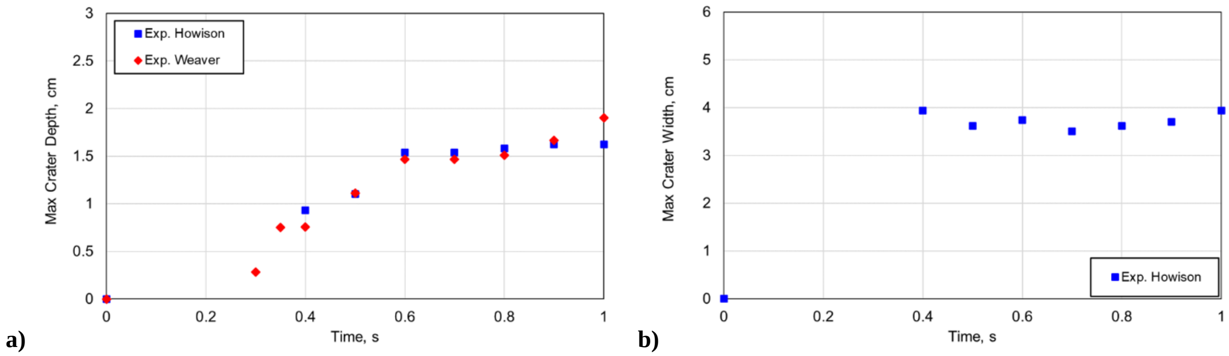

Fig. 8 Maximum a) crater depth and b) width as a function of time during PFGT-1 Run 56. Only the first second of the test is shown.

IX. Computational Mesh

The PFGT-1 test was devised as a symmetric-half model of the real-life three-dimensional PSI event. The sharp-edged splitter plate is coplanar with the nozzle centerline, which bisects the soil bin and nozzle. For computational efficiency, only the half of the domain that contains the plume entering the soil bin was retained. The resulting geometry is shown in Fig. 9. Prior to settling on this 180-degree computational domain, 2D axisymmetric and 90-degree computational domains were explored in pursuit of computational savings. However, it was determined that these reduced domains did not offer the simulation enough degrees-of-freedom to robustly model the unsteady and asymmetric cratering process. In the next phase of validation assessment, the full domain will be retained.

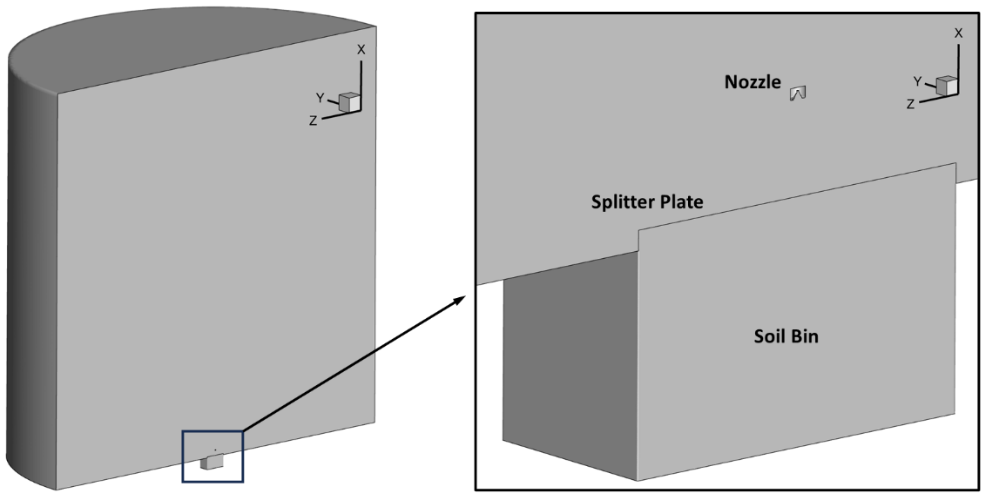

Fig. 9 Geometry of the 180 degree computational domain.

The computational domain outer surface is one-half of a 4.99 m radius cylinder. The top of the splitter plate is located at 0.026 m above the soil bed. The simulated h/D relative to the initial soil level as initialized in the simulation is 10.76. This does not match the actual value of 10.33 for Run 56. The h/D will be carefully matched to each PFGT-1 test in the next phase of validation assessment.

The computational mesh along the $y = 0$ plane is shown in Fig. 10. The soil bin and the region directly above it contained a structured mesh to enable high quality meshes in the region when adaptive mesh refinement (AMR) was used. An integrated AMR has been a primary feature of the vision to allow efficient application of Loci/GGFS to PSI applications. The purpose of AMR is to identify cells where a marker function, usually a gradient-base error estimate, exceeds a threshold and that cell is marked for subsequent refinement. This marking and refinement process is repeated as the transient PSI simulation progresses with the number of timesteps between successive refinements specified by the user. Both refinement and de-refinement thresholds are controllable within the input deck of Loci/GGFS. The volume mesh without AMR cells contained over 11 million cells. With AMR, the cell count increased to around 50 million cells.

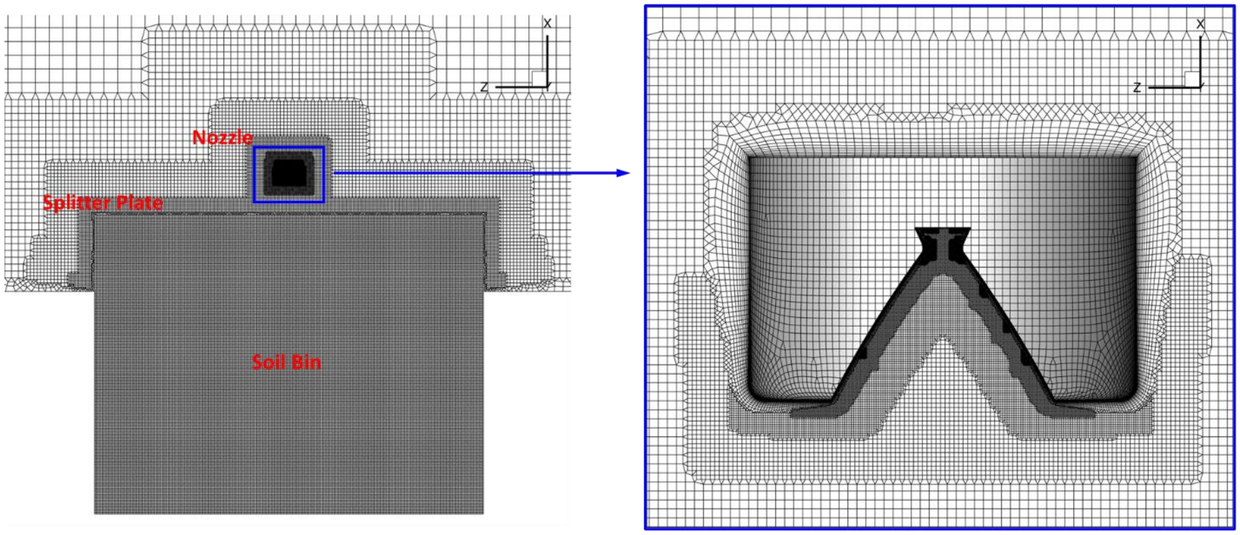

Fig. 10 Computational mesh on $y = 0$ plane.

X. Simulation Settings

The outer computational domain boundaries are set to the experimental outflow condition with a pressure of 267 Pa. The $y = 0$ symmetry plane is set to the reflecting condition. The nozzle inlet boundary condition was set to a temporally ramped fixed mass flow rate of 1.6×10^{-4} kg/s of nitrogen gas over 0.15 seconds, which corresponds to half of the full nozzle flow rate (only half of the full geometry is modeled). The linearly ramped inflow condition is a known idealization of the experimental ramp that will be explored in future work. All solid surfaces, except for the nozzle internal flow surface, are set to viscous wall conditions with a fixed temperature of 288 K for the soil bin and 500 K for the nozzle block.

The nozzle wall is set to the reflecting condition. The choice was made to retain the reflecting condition in this work in order to maintain consistency with previous PFGT-1 simulations. Turbulence modeling was not active in any of the results presented in this work. Sensitivity to the nozzle wall condition combined with the use of a turbulence model will be explored in future work. The simulation initial condition was quiescent nitrogen gas with a pressure of 267 Pa and a temperature of 288 K. Simulations were executed with time steps of ranging from 5.0×10^{-6} to 1.0×10^{-5} s.

XI. Monodisperse Glass Beads (MGB) Results

The monodisperse glass bead simulation was executed to 0.819 seconds. It is instructive to examine the crater evolution through time to get a sense for how the plume and soil evolve. Only an abridged version of the MGB results is presented in this paper since Run 56 used BP-1 soil. All presented MGB results were generated using AMR. Fig. **11** contains six instances in time from the simulation, with contours of Mach number and the base 10 logarithm of the solid volume fraction displayed on a $z = 0$ slice through the computational domain. The $z = 0$ plane contains the nozzle centerline and extends in the positive y-direction into the soil bin. The first signs of erosion occur at 0.05 seconds when the nozzle flow rate is one-third of its nominal value. At this time, the boundary layer originating at the splitter tip is visible, and the plume expands radially outward, hugging the soil surface. By the time the nozzle is flowing its full flowrate at 0.15 seconds, a significant crater has formed with two distinct ejecta streams: one heading vertically upwards outboard of the nozzle and the other heading outboard with a small angle upward. In addition, the recirculation bubble between the main impingement location on the surface and the splitter plate has deposited displaced soil against the splitter plate to a height well above the initial soil surface. At 0.25 seconds, the crater has grown deeper, and the strength of the upwards ejecta stream has abated some and increased in width. The outboard stream has lengthened and become more parallel to the soil surface. The height of the displaced soil against the splitter plate has decreased, yet it is still above the initial soil surface.

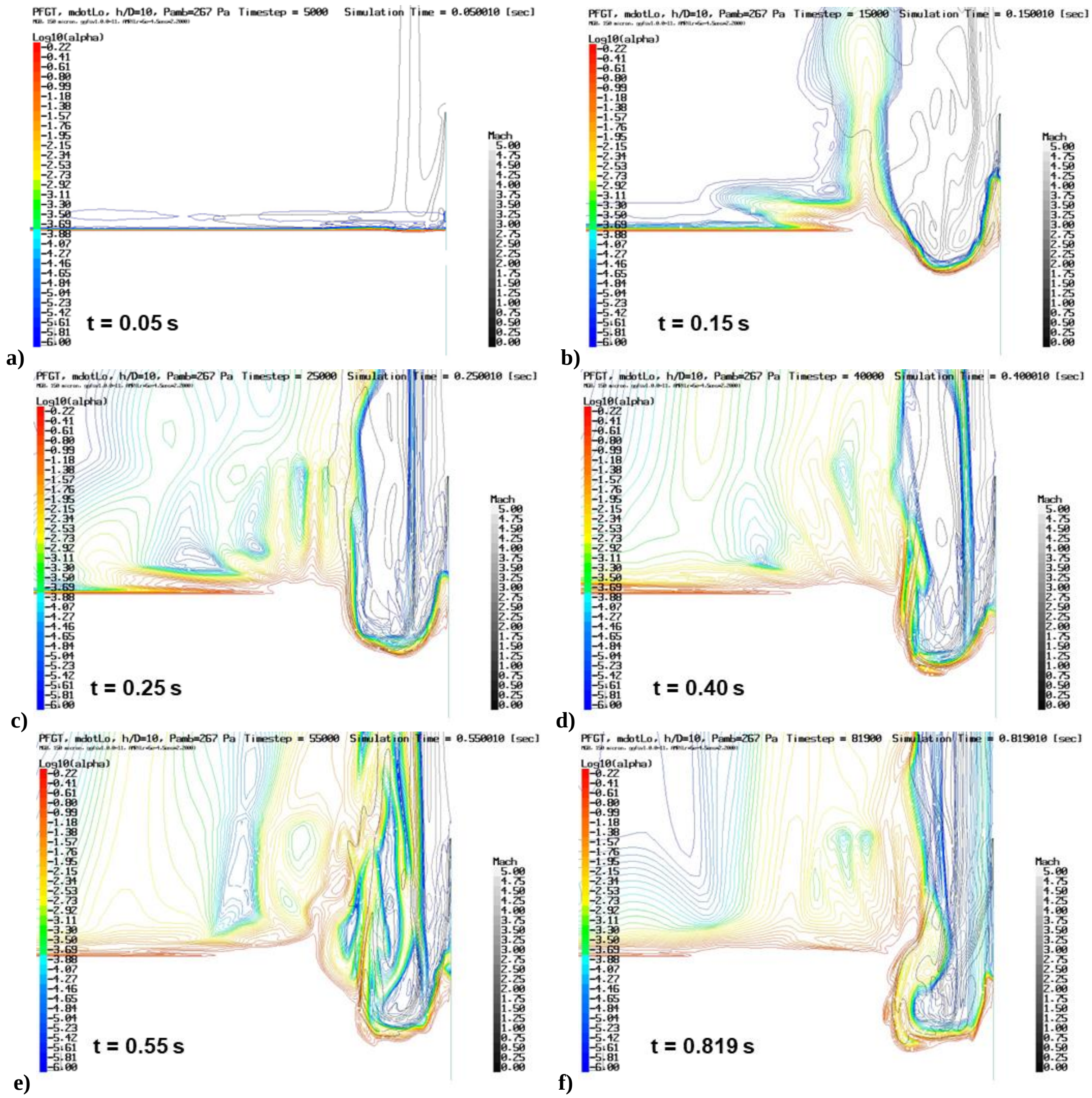

Fig. 11 Six instances in time, 0.05, 0.15, 0.25, 0.40, 0.55 and 0.819 seconds, showing contours of Mach number and the base 10 logarithm of the solid volume fraction displayed on a *z* = 0 slice through the computational domain.

The ejecta streams have nearly merged by 0.4 seconds after forming a significant outboard berm, which was observed since 0.15 seconds. A new ejecta stream has become evident, this one moving downwards. Evidence of this stream is present at 0.25 seconds and continues to grow stronger as the simulation progresses. The height of displaced soil against the splitter plate has reduced to a value less than the initial height of the soil. The crater depth at 0.55 seconds is only slightly deeper than at 0.4 seconds but with a greater width in the outboard direction. Only one outboard flowing ejecta stream is visible, and it is mostly upwards with a slight angle towards the plume. The soil concentration within the downward jet has increased substantially as well as increased in width in the *y*-direction. The height of displaced soil on the splitter plate has decreased somewhat from the previous time. At 0.819 seconds, the outward ejecta streams have merged but now are directed mostly upwards. The downward ejecta stream has now moved to include the centerline of the plume. The crater has not increased substantially in depth but has increased in width in the *y*-direction. The height of the displaced soil against the splitter plate has not changed significantly from the previous time.

Six instances in time are shown in

Fig. **12** of a solid volume fraction isosurface of 0.275 in a side view corresponding to the crater camera view present in the PFGT-1 experiments. A grid of lines are rendered to aid in quantifying the crater maximum depth and the maximum crater width along the splitter plate. In this view, the complexity of the crater shape is more visible with bimodal cups appearing. There is also direct evidence of diffusion-driven erosion. A slightly altered visualization was created to further aid in quantifying the maximum crater depth and width on the splitter plate. The alteration was that the isosurface was only rendered in a thin layer adjacent to the splitter plate. An example of this visualization is shown in Fig. 13. The results in Fig. 13 highlight the challenge in comparing the experimental crater depth and width with simulations. Overhead cameras were present during the PFGT-1 experiment, but they cannot provide a quantitative measure of depth due to viewing angle and dust obscuration during the experiment. In this paper, the maximum crater depth and the maximum crater depth along the splitter plate are reported. The experimental values were obtained from measurements along the splitter plate as discussed in the Validation Data Selection section of the paper.

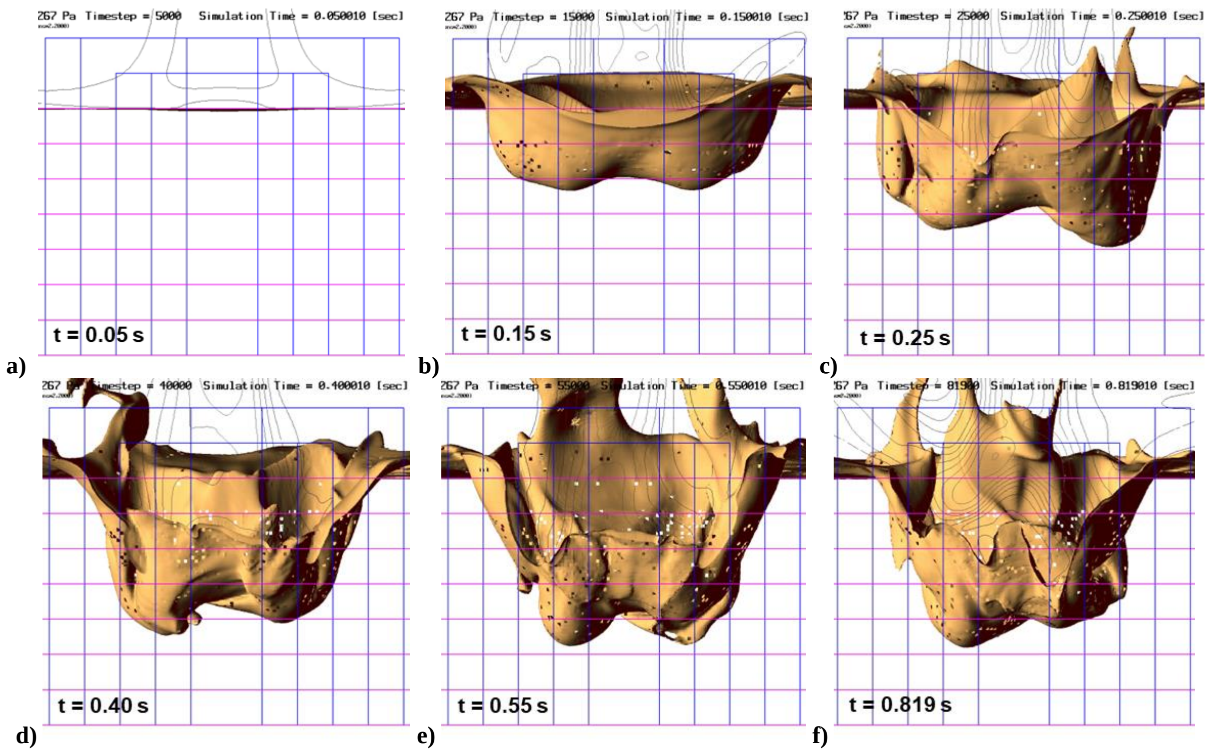

Fig. 12 Six instances in time, 0.05, 0.15, 0.25, 0.40, 0.55 and 0.819 seconds, showing a solid volume fraction isosurface of 0.275. Rendered grid lines are 5 mm apart to aid in quantifying crater dimensions.

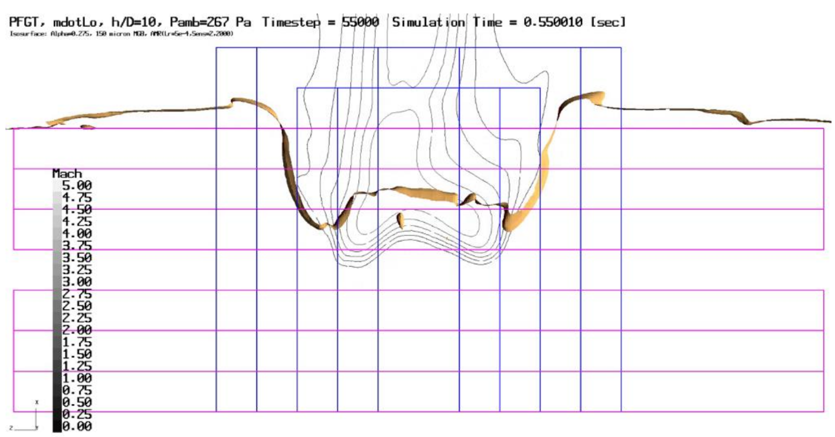

Fig. 13 Altered version of a visualization in Fig. 12 limiting the isosurface rendering to a thin layer adjacent to the splitter plate.

The evolving maximum crater depths and width as a function of time are shown in Fig. 14. The left plot shows the maximum depth and the maximum depth along the splitter plate from the simulation along with results from PFGT-1 Run 56 for reference. The right plot shows the crater width from the simulation along with the result from PFGT-1 Run 56 for reference. The maximum crater depth grows rapidly to 0.02 m by 0.25 seconds and then asymptotes to approximately 0.024 m by 0.6 seconds. The maximum depth along the splitter plate deviates from zero at about 0.15 seconds and quickly grows to 0.01 m by 0.25 seconds. By 0.3 seconds the depth has exceeded 0.015 m and oscillates around an average of approximately 0.013 m. Note that at early times, as depicted in Fig. 11, a berm of displaced soil is formed along the splitter plate corresponding to negative depths. These have been omitted here for clarity. The crater width deviates from zero at about 0.15 seconds and quickly grows to 0.038 m by 0.25 seconds where it oscillates around for the remainder of the simulation.

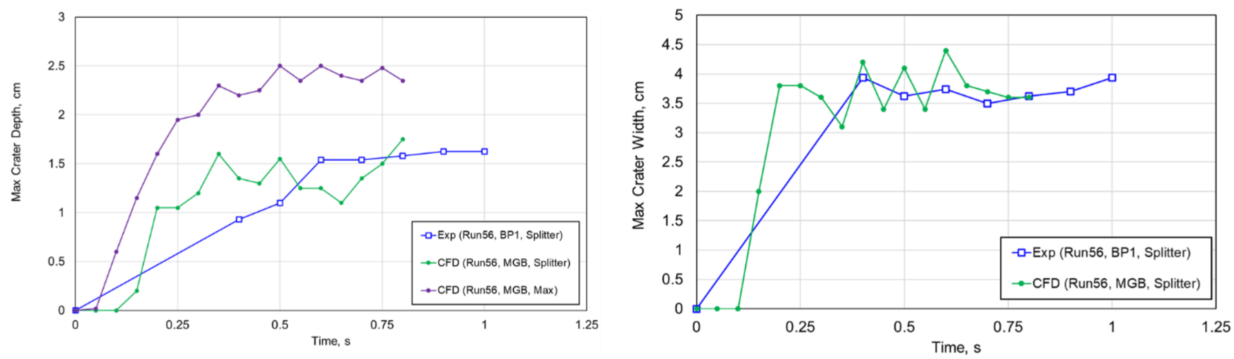

Fig. 14 Altered version of the previous visualization limiting isosurface rendering to a thin layer adjacent to the splitter plate.

Conditions corresponding to Run 56 were not tested using the MGB soil in the PFGT-1 test series. The Run 56 simulations using MGB soil produce a crater depth at the splitter plate consistent, within about 16 percent, with those of the Run 56 experiment which used the BP-1 Lunar soil simulant. The simulation crater width is closer to the Run 56 experiment with the asymptotic value within about 10 percent different than experiment. The sensitivity of the results to the soil model will be discussed after the BP-1 soil model results are presented.

XII. Monodisperse BP-1 Soil Model Results

The monodisperse BP-1 soil simulation was executed to 1.0 seconds. Fig. **17** contains six instances in time, with contours of Mach number and the base 10 logarithm of the solid volume fraction displayed on a z = 0 slice through the computational domain. The z = 0 plane contains the nozzle centerline and extends in the positive y-direction into the soil bin. The ejecta patterns are qualitatively similar to the MGB simulation (Fig. 11). In this cut plane for the monodisperse BP-1 soil model, however, the crater width does appear slightly smaller and the vertical ejecta stream is slightly more pronounced than was shown in the MGB soil model results.

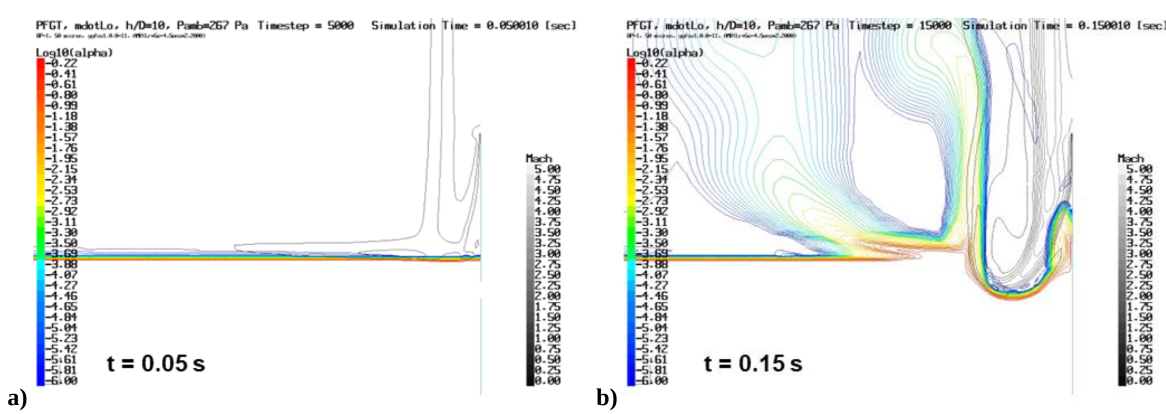

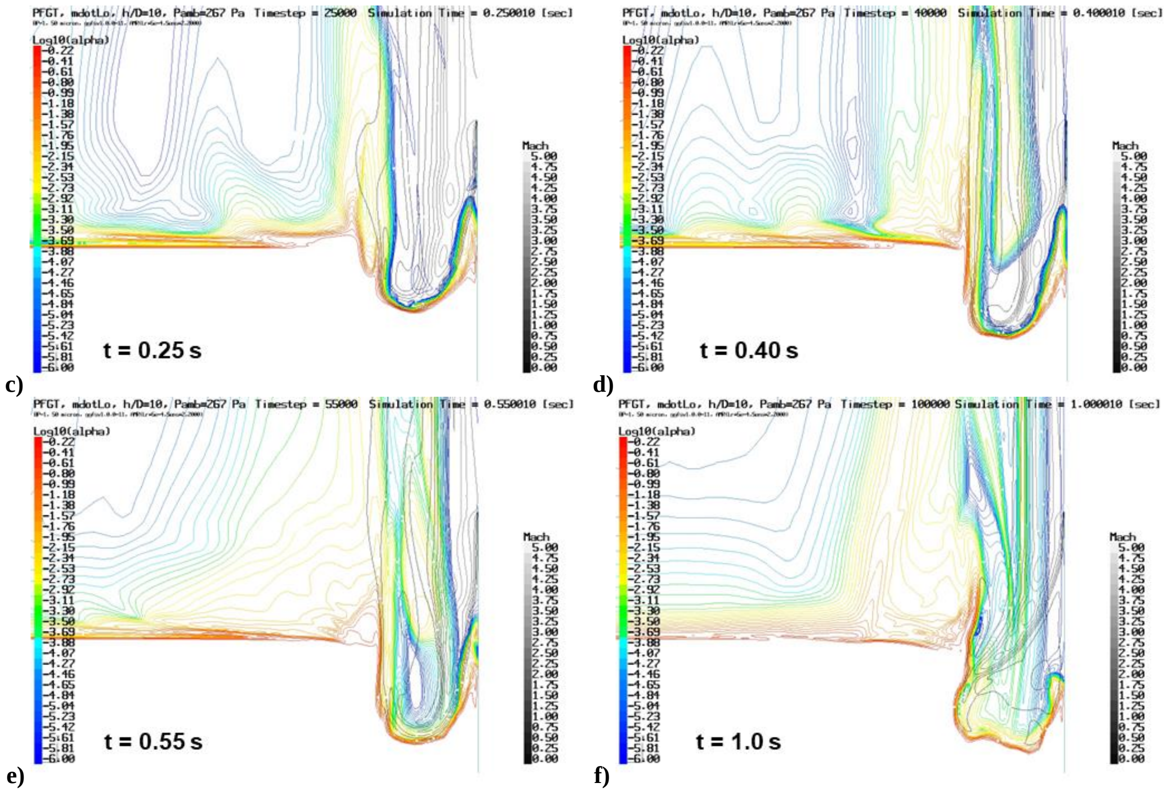

Fig. 15 Six instances in time, 0.05, 0.15, 0.25, 0.40, 0.55 and 1.0 seconds, showing contours of Mach number and the base 10 logarithm of the solid volume fraction displayed on a *z* = 0 slice through the computational domain.

The evolution of the mesh created by the AMR refinement is shown in Fig. 16. The layout of this figure is the same as Fig. 15 except that the Mach contours are omitted, and the mesh is rendered. At 0.05 seconds the mesh at the soil surface has been refined to the specified edge length threshold which results in a spacing of 0.33 mm. The plume region has also been refined with the recirculation anchored at the splitter plate time affecting the mesh refinement pattern. Note that the mesh refinement extends several layers, 8 to 12, deeper into the soil than the crater depth as indicated by the soil volume fraction. This correspondence is maintained throughout the simulation and is a direct result of the refinement marker function design. The mesh refinement has reached full development by 0.4 seconds and follows the small increases in depth and width after this time.

The small 'pockmarks' in the mesh distribution are noted. These are instances where the surrounding mesh of a single cell has exceeded the edge length threshold and have been refined one more level than the single cell. This behavior is not optimum for numerical stability and solution accuracy and should be addressed in the future.

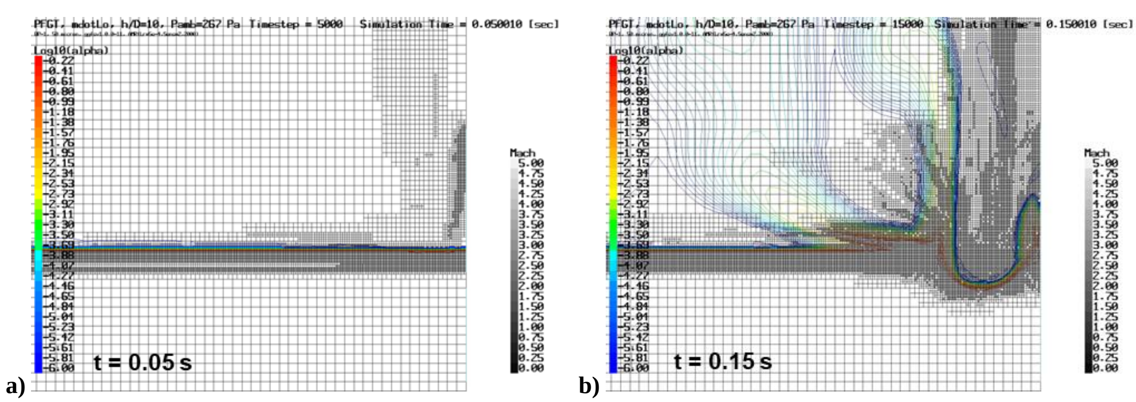

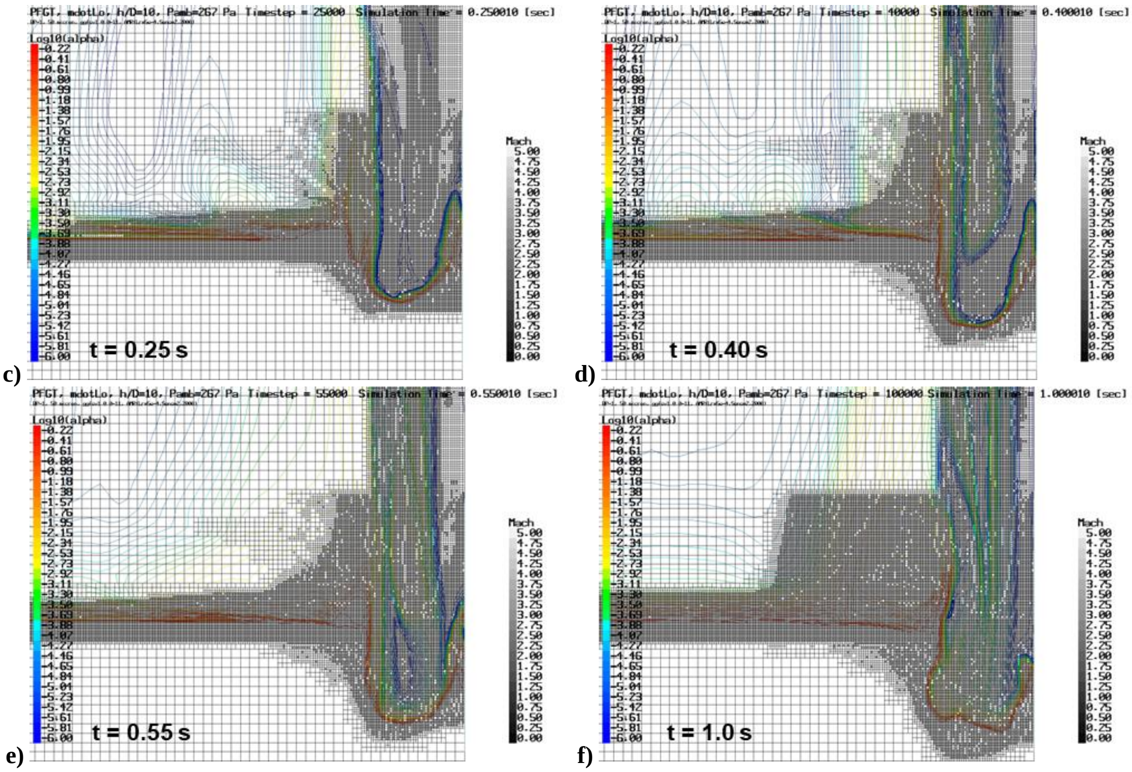

Fig. 16 Six instances in time, 0.05, 0.15, 0.25, 0.40, 0.55 and 1.0 seconds, showing contours of Mach number and the base 10 logarithm of the solid volume fraction displayed on a *z* = 0 slice through the computational domain.

Six instances in time are shown in Fig. 17 with contours of Mach number and the base 10 logarithm of the solid volume fraction and a solid volume fraction isosurface of 0.275 displayed in an isometric view of the soil bin and nozzle region. Features in addition to those described in the previous figures include the clear evidence of diffusion-driven erosion from 0.15 seconds onwards as well as the full view of the recirculation of the upward ejecta stream to form the downward stream described previously. The complex pattern of soil berm formation is also evident in this figure.

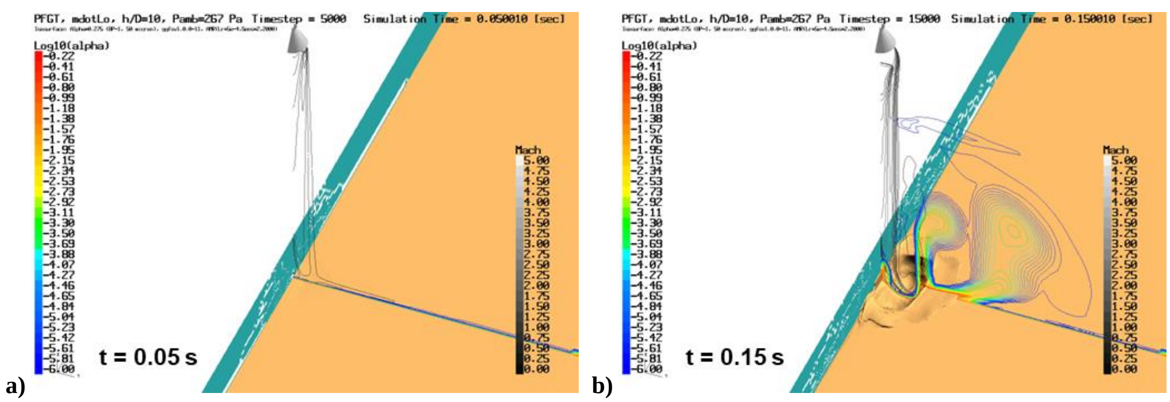

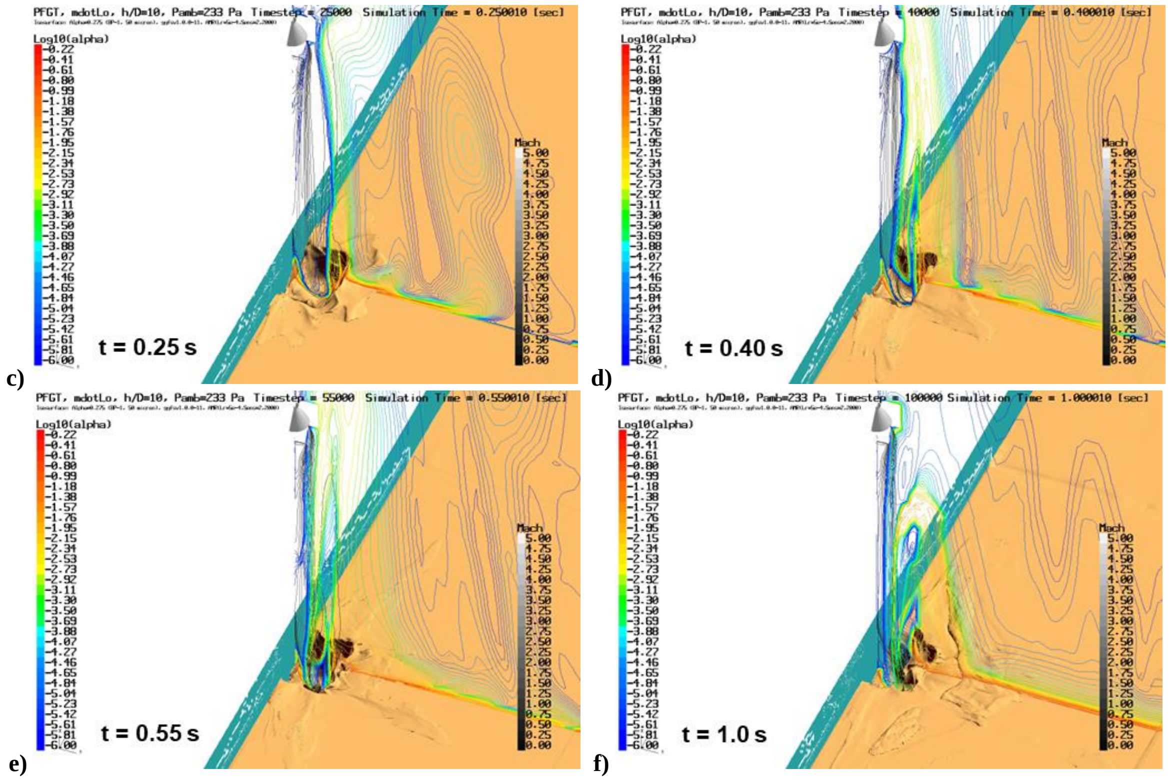

Fig. 17 Six instances in time, 0.05, 0.15, 0.25, 0.40, 0.55 and 1.0 seconds, with contours of Mach number and the base 10 logarithm of the solid volume fraction and a solid volume fraction isosurface of 0.275.

Six instances in time are shown in Fig. 18 of a 0.275 solid volume fraction isosurface colored by vertical distance relative to the initial soil height in a top view from above the nozzle. Positive values represent berm formation and negative values represent local crater depth. The internal crater shape becomes more complex as time progresses exhibiting bimodal cups in the bottom of the crater at times. The diffusion driven erosion ejecta streams are present at the edges of the crater and are transient in nature and location. The complex flow pattens and soil deposition are visible in this figure.

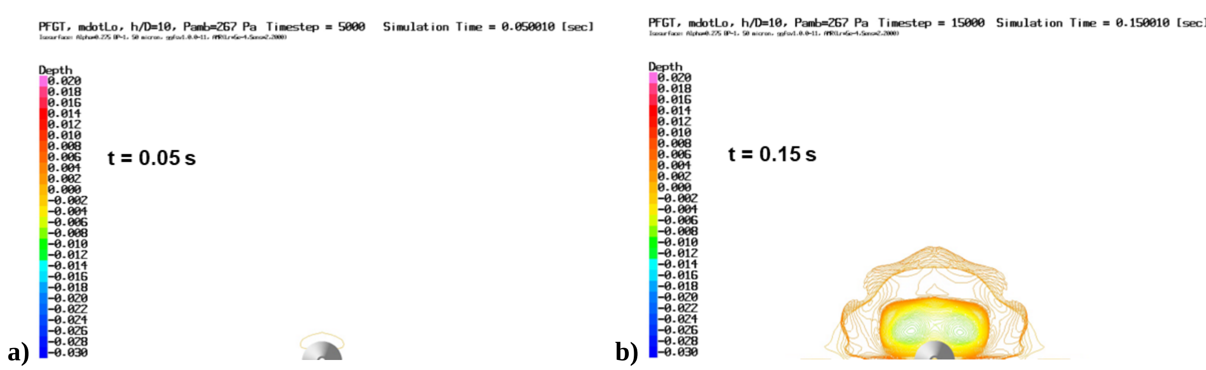

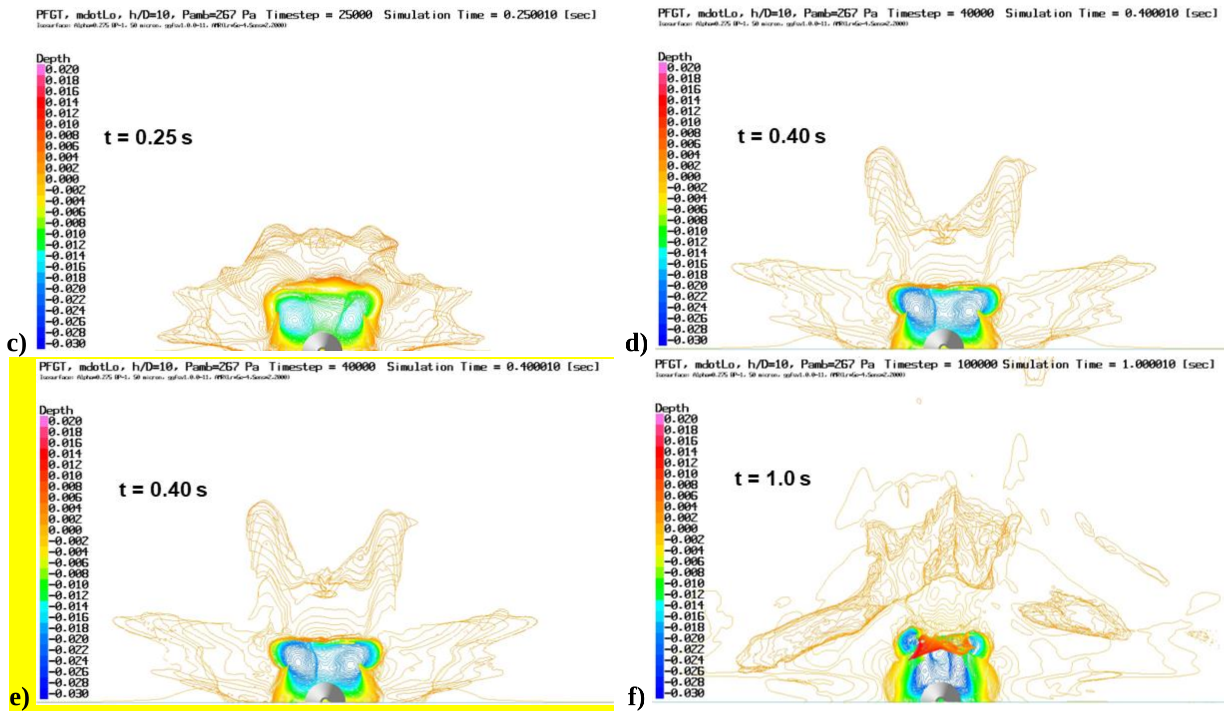

Fig. 18 Six instances in time, 0.05, 0.15, 0.25, 0.40, 0.55 and 1.0 seconds, of a 0.275 solid volume fraction isosurface colored by the isosurface vertical distance relative to the initial soil height in a top view from above the nozzle.

Fig. 19 contains six instances in time of a 0.275 solid volume fraction isosurface in a top view above the nozzle. Additional views of the evidence of diffusion-driven erosion from 0.15 seconds onwards and the complex pattern of soil berm formation are visible.

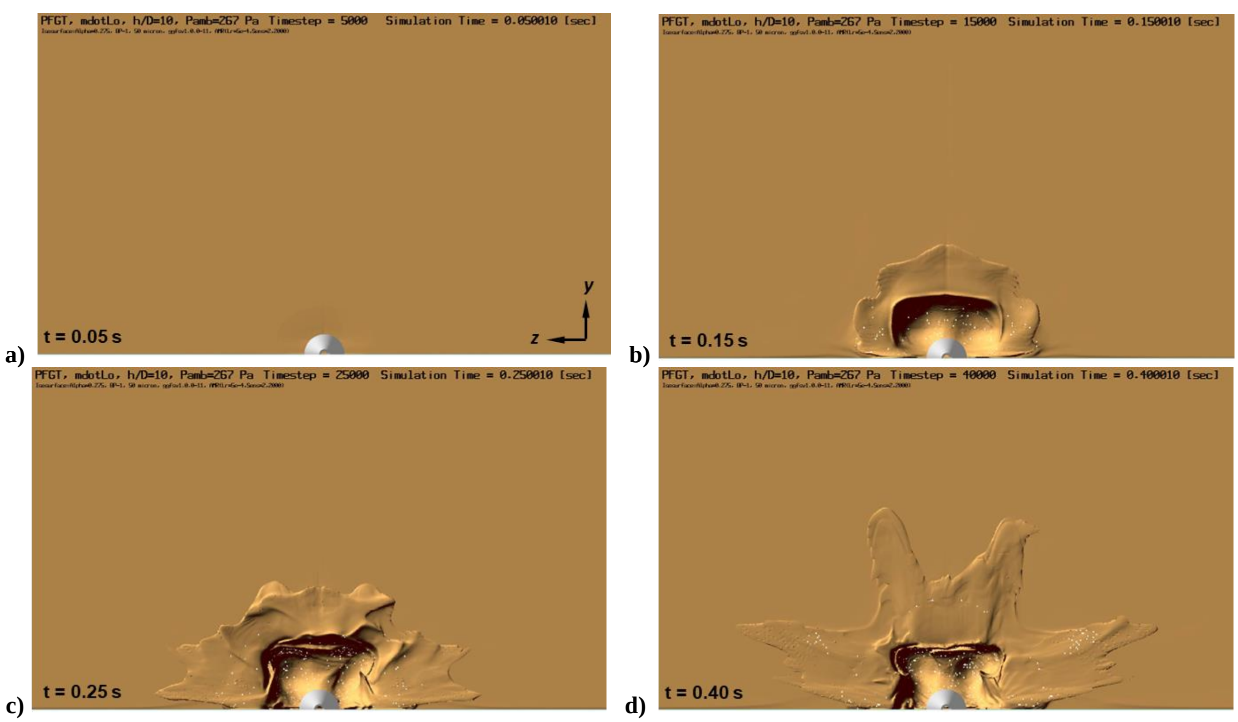

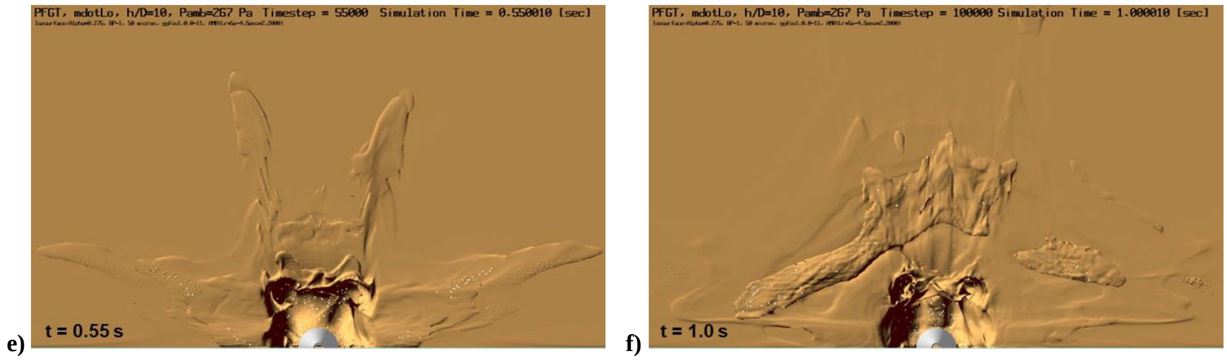

Fig. 19 Six instances in time, 0.05, 0.15, 0.25, 0.40, 0.55 and 1.0 seconds, of a 0.275 solid volume fraction isosurface in a top view above the nozzle.

Six instances in time are shown in Fig. 20 of a 0.275 solid volume fraction isosurface in a side view corresponding to the crater camera view present in the PFGT-1 experiments. A grid of lines spaced at 0.005 m are rendered to aid in quantifying the crater maximum depth and the maximum crater depth along the splitter plate. The bimodal cups mentioned in previous figures are visible as well as direct evidence of diffusion-driven erosion. A slightly altered visualization was created to further aid in quantifying the maximum crater depth and width on the splitter plate. The alteration was that the isosurface was only rendered in a thin layer adjacent to the splitter plate. An example of this visualization is shown in Fig. 21.

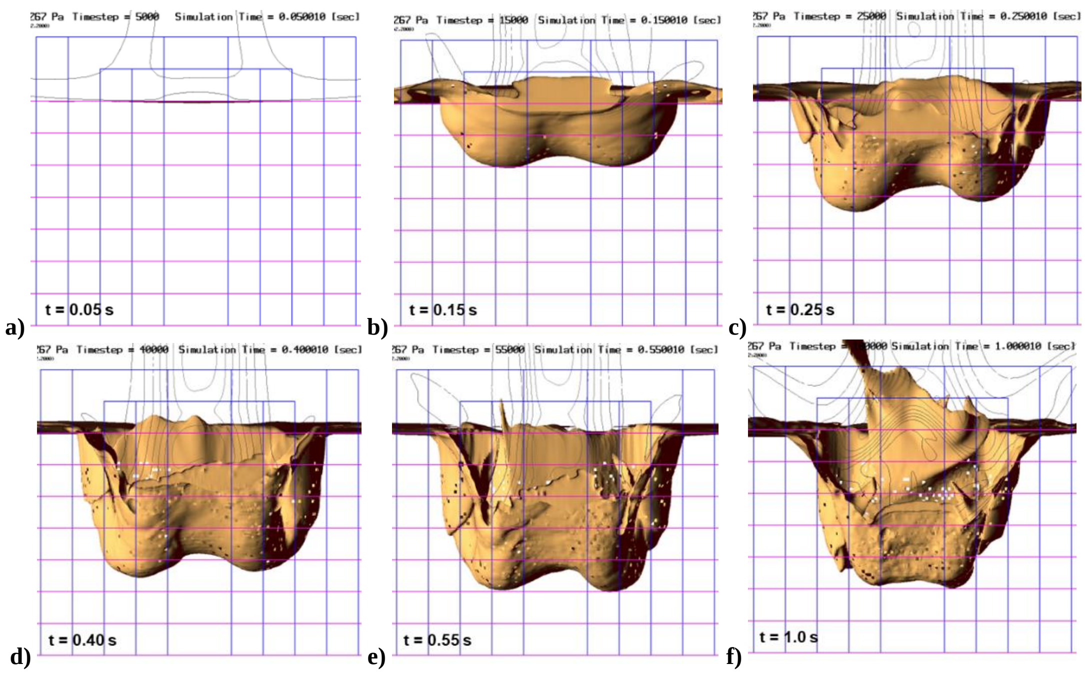

Fig. 20 Six instances in time, 0.05, 0.15, 0.25, 0.40, 0.55 and 1.0 seconds, showing a solid volume fraction isosurface of 0.275. Rendered grid lines are 5 mm apart to aid in quantifying crater dimensions.

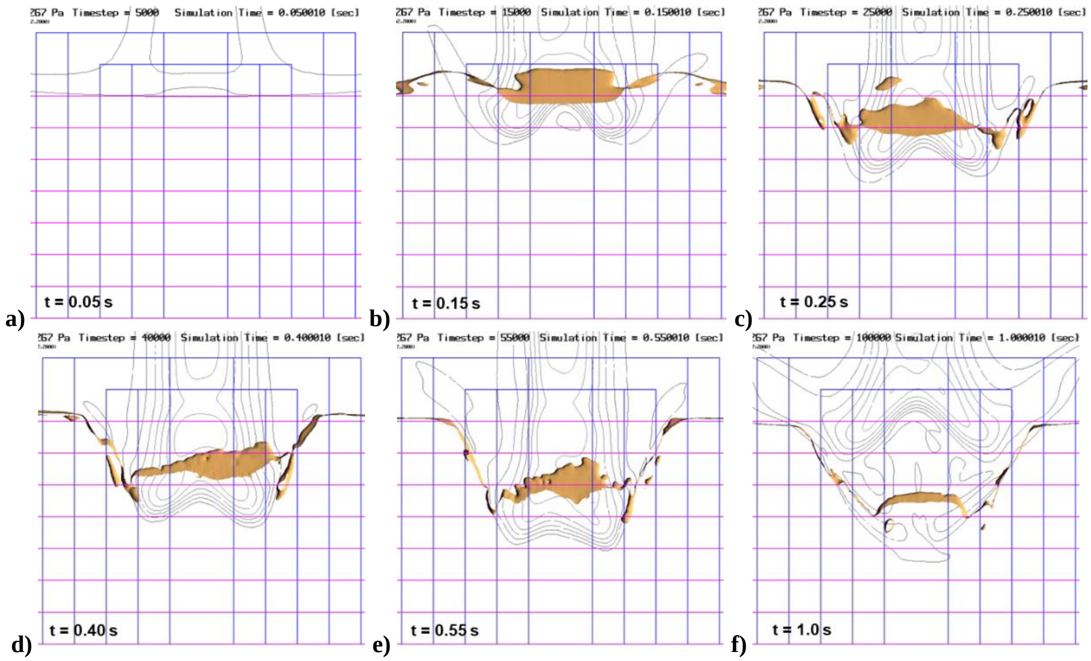

Fig. 21 Altered version of a visualization in Fig. 20 limiting the isosurface rendering to a thin layer adjacent to the splitter plate.

The evolving crater depths and width as a function of time are shown in Fig. 22. The left plot shows the maximum depth as well as the maximum depth along the splitter plate from the simulation along with experimental results from PFGT-1 Run 56 for reference. The right plot shows the crater width from the simulation along with the experimental result from PFGT-1 Run 56 for reference. The maximum crater depth grows rapidly to 0.017 m by 0.25 seconds and then asymptotes to approximately 0.026 m by 0.8 seconds before reducing to 0.025 m by 1.0 seconds. The maximum depth along the splitter plate deviates from zero at about 0.15 seconds and quickly grows to 0.005 m by 0.25 seconds. By 0.6 seconds the maximum splitter plate depth has reached 0.015 m and then oscillates about an apparent mean of 0.014 m. Note that at early times, as depicted in Fig. 15, a berm of displaced soil is formed along the splitter plate corresponding to negative depths, which have been omitted here for clarity.

The crater width increases rapidly to about 0.015 m and then reduces to zero. This is likely due to the early formation of berms as described above. Then the width jumps to 0.035 m at 0.2 seconds. The width meanders about an apparent average of 0.0375 m until 0.95 seconds, where it increases rapidly to about 0.055 m.

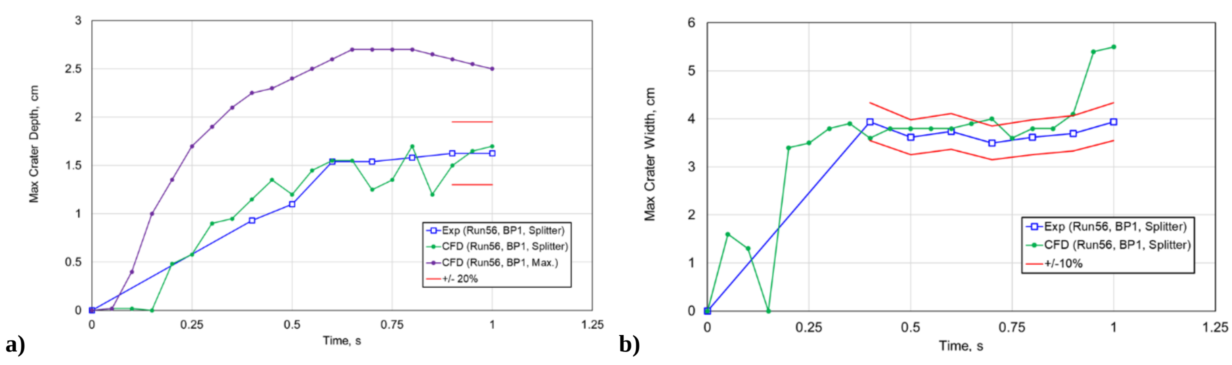

Fig. 22 Crater maximum depth and maximum crater depth along the splitter plate (left) and maximum crater width along the splitter plate (right).

Fig. 22 also contains red lines depicting percent difference from the experimental data. The red lines in the crater depth plot indicate twenty percent less and greater than the last two data points of PFGT-1 Run 56. The red curves in the crater width plot indicate ten percent less than and greater than the experimental data. The crater depth from

Loci/GGFS varies from the test data over a range of about -20% to 0%.This suggest that the mean crater depth on the splitter plate oscillates about a mean that is ten percent less than the experimental data from Run 56 from 0.4 to 1.0 seconds. The crater width on the splitter plate from Loci/GGFS remains within a ten percent range of the Run 56 data from 0.2 to 0.9 seconds. The spike in crater width of the Loci/GGFS crater is a subject for future investigation.

Comparing the BP-1 soil model results in Fig. 22 to the MGB soil model results in Fig. 14, the biggest difference is the rate of initial cratering. The MGB soil model is close to its maximum depth by 0.35 s and maximum width by 0.2 s. The BP-1 soil model is delayed relative to the MGB soil model. It approaches its maximum depth by 0.6 s and maximum width by 0.35 s. This makes sense in terms of particle shapes since the BP-1 soil model contains the shape complexity shown in Fig. 1. Compared to the spherical MGB particles, the BP-1 particles have more ability to interlock and resist erosion.

XIII. Mesh and Spatial Order of Accuracy Sensitivity Study

The previous section described the results with AMR activated. The working assumption is that a properly specified AMR approach will produce equivalent results to a fine enough static, uniform mesh. Additionally, the robustness of the Loci/GGFS tool has yet to reach a reliable production-ready state. Experience has shown that reverting the spatial order of accuracy from the baseline second order to first order results in significantly less divergences of the Loci/GGFS simulations. This section describes the assessment of sensitivity to mesh and spatial order of accuracy.

A. Mesh Sensitivity Study

Six different computational meshes used for the mesh sensitivity and spatial order of accuracy assessments are shown in Fig. 23. From left to right and top and then bottom, the six meshes are: a) the baseline mesh, b) the baseline mesh refined one level in a specified region, c) the baseline mesh refine twice in the same specified region, d) the baseline mesh refined three times in the same specified region, e) the baseline mesh and solution described in the previous sections, and f) the baseline mesh with AMR identical to that in the previous section but with spatial order of accuracy set to one instead of two. The region used for static mesh refinement was similar to that used to define refinement regions for the simulations using AMR. The mesh state/size at the end of each simulation were: a) static/11,468,507, b) static/13,116,796, c) static/22,776,789, d) static/42,148,589, e) AMR/45,665,062, and f) AMR/40,517,278 cells, respectively.

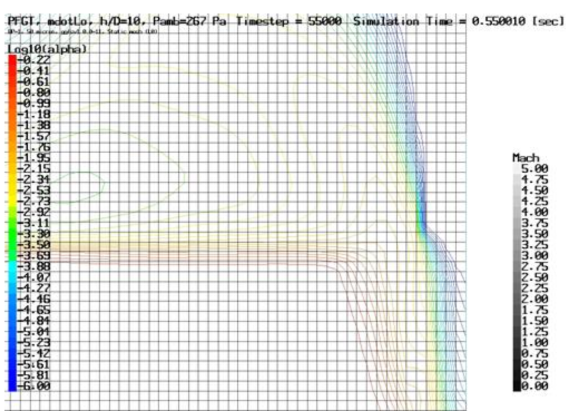

a)

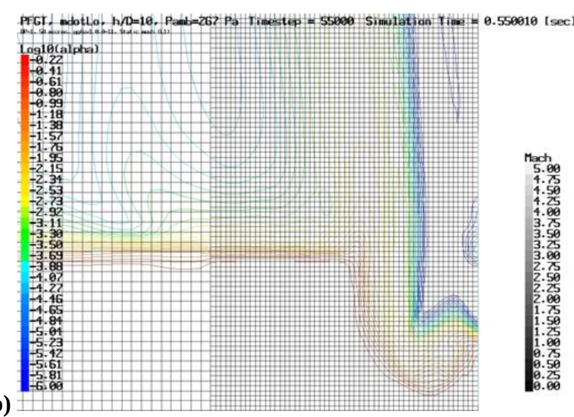

b)

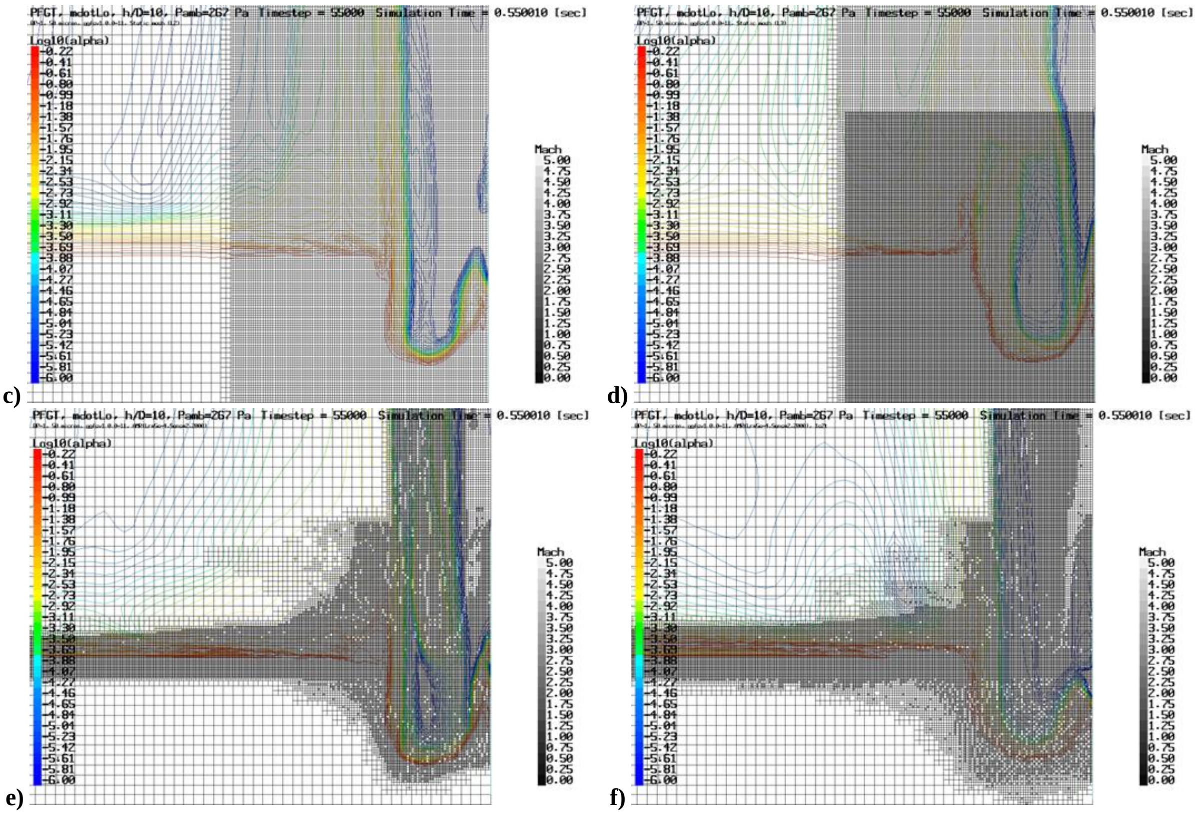

Fig. 23 Contours of the base 10 logarithm of the solid volume fraction and the computational mesh displayed on a z= 0 slice through the computational domain for six different meshes at a simulation time of 0.55 seconds.

Fig. 24 shows all six simulation results at 0.55 seconds with contours of Mach number and the base 10 logarithm of the solid volume fraction and a 0.275 solid volume fraction isosurface displayed in an isometric view of the soil bin and nozzle region. The static baseline mesh clearly results in an overprediction of the crater size. The first level of refinement reduces the size but fails to produce a crater edge shape like that of the baseline AMR mesh. The second and third levels of refinement both produce a crater shape similar to the baseline AMR mesh. The second and third levels of refinement also produce similar ejecta stream patterns. The reduction of spatial order from two to one results in a crater shape similar to that of the first level refined static mesh. However, a significant change in ejecta stream pattern is evident.

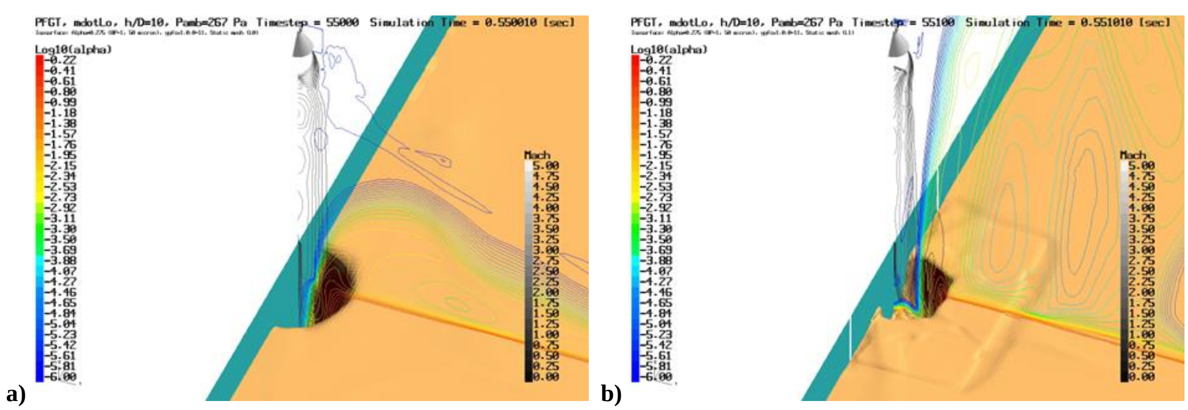

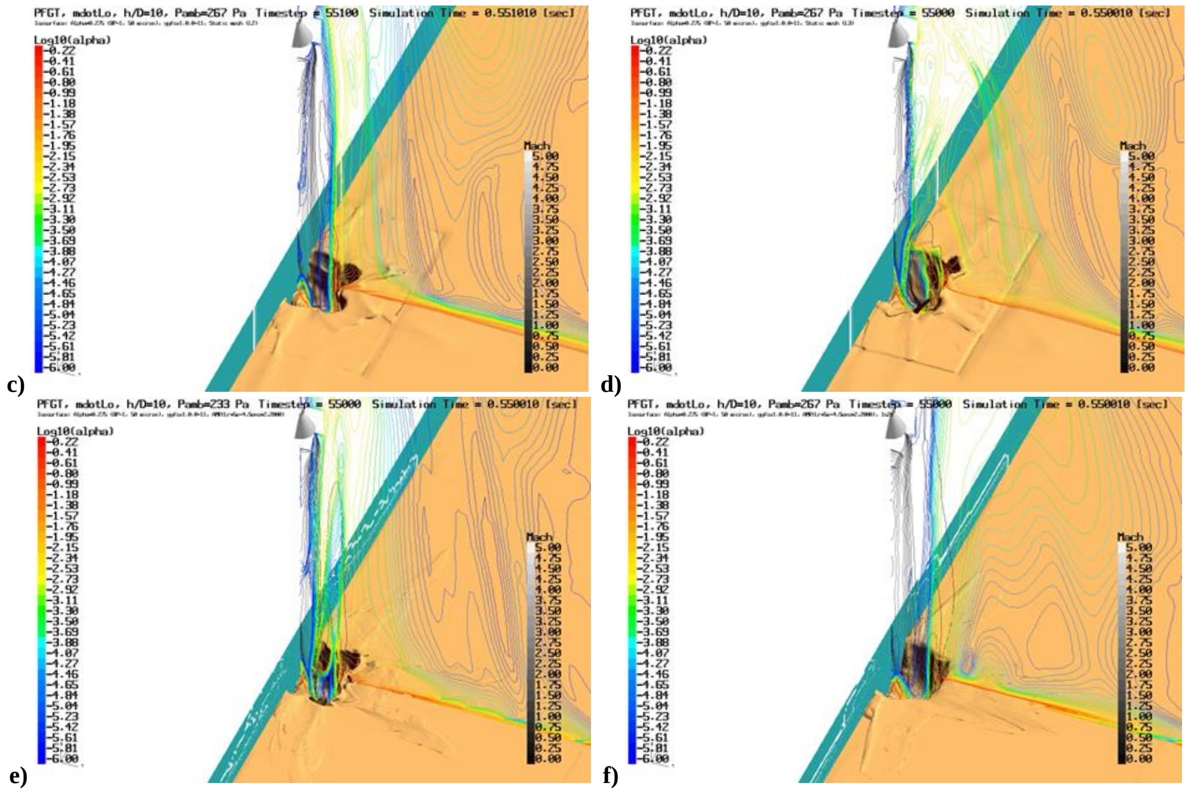

Fig. 24 Contours of Mach number and the base 10 logarithm of solid volume fraction and a 0.275 solid volume fraction isosurface for six different meshes at a simulation time of 0.55 seconds.

Fig. 25 shows a PFGT-1 synthetic crater camera view of the 0.275 solid volume fraction isosurface representing the soil surface for all six simulations at a simulation time of 0.55 seconds. The baseline mesh significantly overpredicts the crater width and depth and fails to capture the qualitative double cup-shaped bottom of the crater and diffusion-driven erosion features. The first level of refinement reduces the crater depth to the ballpark of the most refined mesh results and recovers the double cup feature, but it fails to resolve the diffusion driven erosion features. The second and third levels of mesh refinement produce similar crater depth and width as well as the double cup and diffusion-driven erosion features. The AMR mesh with first order spatial resolution settings produces similar crater depth and width as well as retains the double cup crater shape and less prominent diffusion driven erosion features.

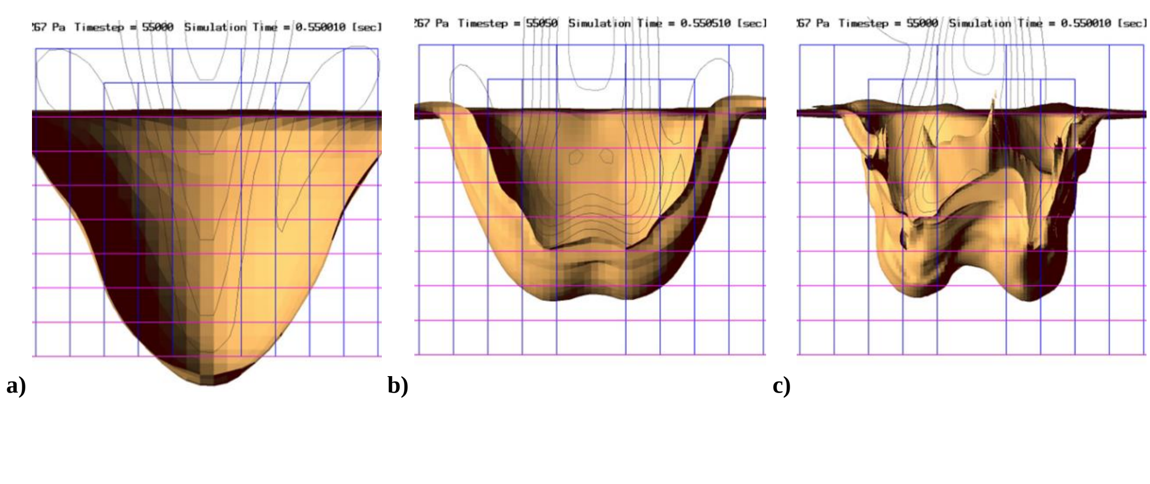

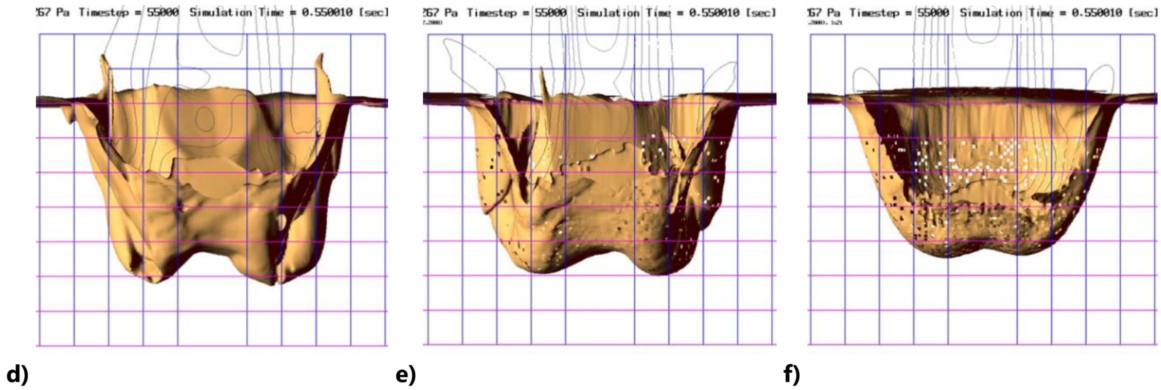

Fig. 25 Solid volume fraction isosurface of 0.275 for six different meshes at a simulation time of 0.55 seconds in a view from above the nozzle.

The maximum crater depth as a function of time for five different meshes are shown in Fig. 26. The baseline mesh simulation produces a crater depth significantly greater than any other mesh, and it is shown only to 0.6 seconds as a result. All other meshes produce a close grouping to 0.65 seconds, where the third level refined mesh simulation was terminated. Increased mesh refinement reveals a reduction in crater depth from 0.8 seconds onwards, with increasing mesh resolution resulting in a greater rate of decrease.

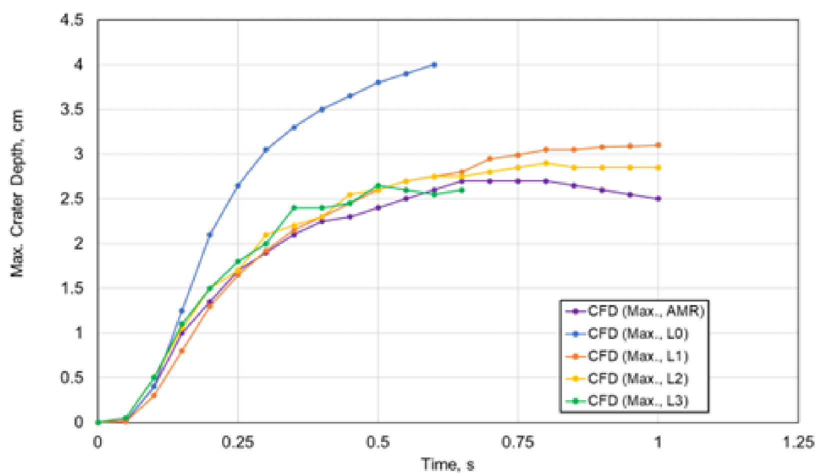

Fig. 26 Maximum crater depth for five different meshes as a function of time.

The maximum crater depth on the splitter plate as a function of time for five different meshes is shown on the left in Fig. 27. The experimental results from PFGT-1 Run 56 are also included. As with maximum overall crater depth, the baseline mesh simulation produces a splitter plate crater depth significantly greater than all other meshes. The first and second level mesh refinements produce depth histories that are consistent with each other and a little above the experimental data. The third-level mesh refinement and the AMR mesh produce consistent depth results which agree well with the experimental data. The difference between the third level refinement, whether static or AMR, and the first and second level refinement is about 25 percent. This outcome motivates a future assessment of a fourth level of mesh refinement. By comparing Fig. 26 and Fig. 27a, it is worth noting that crater depth dependency on the mesh is not confined locally to the splitter plater region or overall maximum crater region. The mesh must be sufficiently fine in any region where crater occurs.

The crater width on the splitter plate is shown on the right in Fig. 27 as a function of time for five different meshes. The experimental crater width from PFGT-1 Run 56 is included. The baseline mesh predicts a width significantly greater than the other meshes and the experimental data. All other meshes produce a relatively close grouping of crater widths with two instances to note. The first is an out of family perturbation of the third level refined mesh at 0.5 seconds, and the second is a systematic increase in width beginning at 0.95 seconds for the AMR mesh. The first instance is associated with a fluidized clump of soil exiting the crater near the location where the soil width is determined. This is an expected feature of diffusion driven erosion. Exploration of the second instance requires simulation to a greater elapsed time, which is a future effort topic.

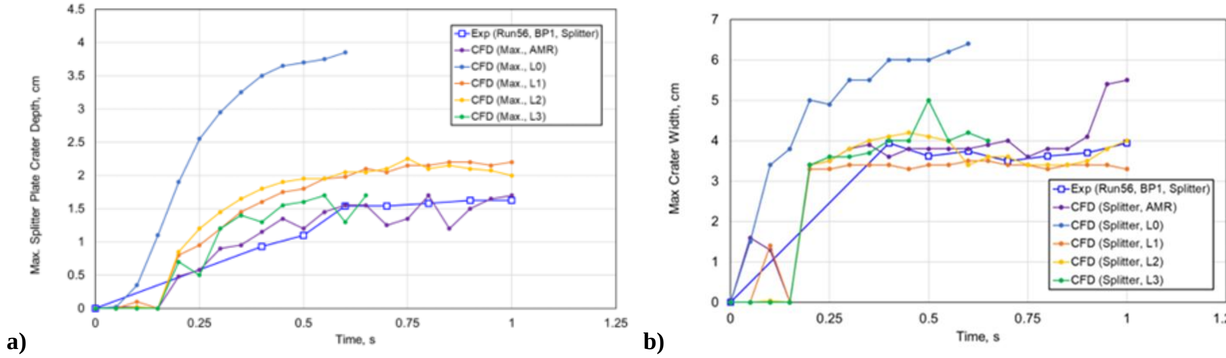

Fig. 27 Maximum crater a) depth and b) width on the splitter for five different meshes as a function of time. Crater depth from PFGT-1 Run 56 is included.

B. Spatial Order of Accuracy Sensitivity Study

It is occasionally advantageous to execute CFD simulations with first order spatial accuracy for improved numerical stability if the metrics of interest do not change significantly. All previous results in this paper were obtained with second order spatial accuracy. In this section, a solution was obtained with first order spatial accuracy using AMR to assess the impact of spatial accuracy on crater depth and width. Mesh sensitivity results from the previous subsection are included in the forthcoming results for ease of comparison across all meshes and solutions.

The maximum crater depth and maximum crater depth on the splitter plate are shown in Fig. 28 as a function of time for five different meshes and the AMR mesh with first order spatial resolution settings in black lines and symbols. The maximum crater width on the splitter plate is similarly shown in Fig. 29. The experimental crater depth and width from PFGT-1 Run 56 is included where appropriate. The first order spatial settings produce a maximum depth that is somewhat less than the finest mesh results. The first order spatial depth on the splitter plate is within the scatter of the finest meshes and slightly above the experimental data. The crater width on the splitter plate from the first order spatial settings is within the scatter of the finest meshes and close to the experimental data. This outcome reveals that quantitatively similar results are expected from first order spatial settings, although incrementally less resolution is expected.

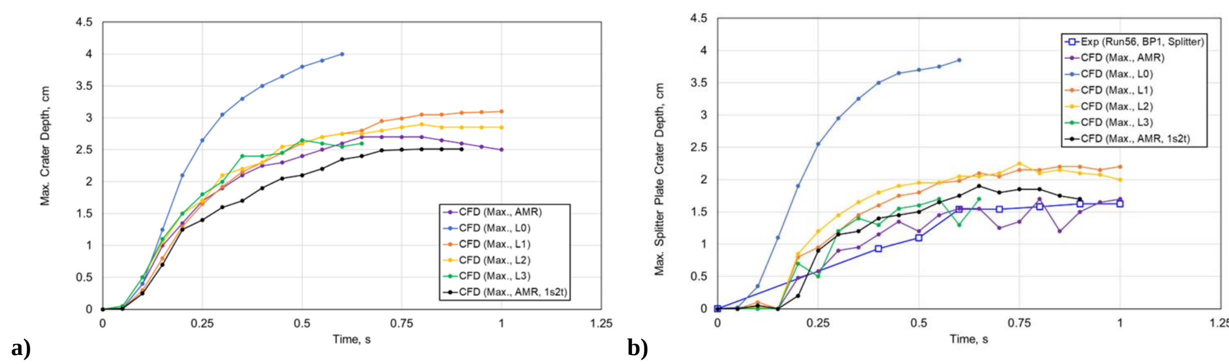

Fig. 28 a) Maximum crater depth and b) maximum crater depth on the splitter for five different meshes and first order spatial settings as a function of time. The crater width and depth from PFGT-1 Run 56 is included.

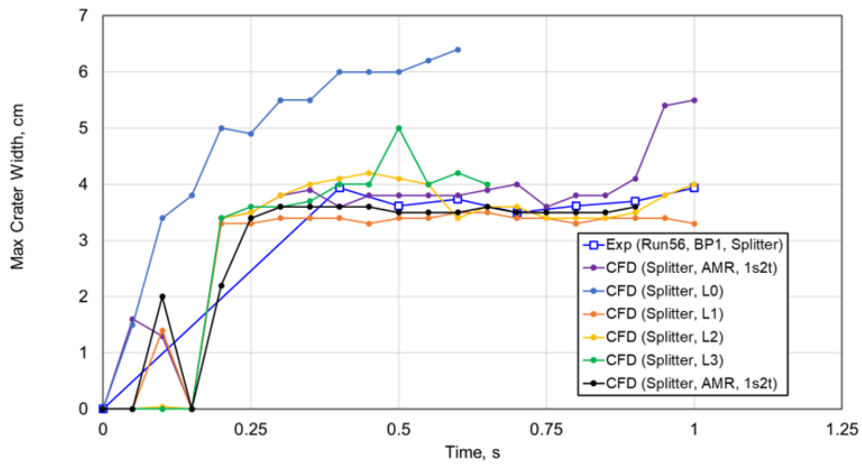

Fig. 29 Maximum crater width on the splitter for five different meshes and first order spatial settings as a function of time. The crater width and depth from PFGT-1 Run 56 is included.

XIV. Summary and Future Validation Plans

The results presented herein represent the initial phase of the Loci/GGFS validation assessment. Crater depth and width predictions were compared with experimental data from PFGT-1 Run 56. The experiment was conducted using BP-1 lunar regolith simulant. Simulations were conducted using an MGB soil model and a monodisperse BP-1 soil model. On AMR meshes, the MGB soil model and BP-1 soil model produced qualitatively similar crater features and maximum depth and width predictions. The MGB crater did increase in maximum depth and width more quickly.

For the MGB soil model, the predicted crater depth along the splitter plate was within 16% of the experiment near the conclusion of the simulation at 0.8 seconds. The predicted crater width was within about 10% of the experimental asymptotic value near 1.0 second. The BP-1 soil model also matched the experimentally observed crater depth and width very well. On the baseline mesh with AMR, the predicted mean crater depth on the splitter plate oscillated about a mean 10% less than the experimental data from Run 56 from 0.4 to 1.0 seconds. The crater width on the splitter plate from Loci/GGFS remains within a 10% range of the Run 56 data from 0.2 to 0.9 seconds. Future work is needed to investigate a spike in the crater width near 1.0 second.

Crater depth and width sensitivity to mesh resolution were studied by comparing results on four successively finer meshes to the baseline AMR results. The coarsest mesh (baseline mesh without AMR) yielded significantly greater crater depth and width predictions than the other meshes or the experiment. First and second level refinement meshes produced similar depth and width predictions with depth overpredicting experiment by about 25%. The third level refinement mesh gave depth and width predictions approaching the baseline AMR mesh and the experiment, but there is reason to investigate a fourth level refinement mesh.

Solution sensitivity to the spatial order of the solver was also explored. The baseline AMR case was executed using first order spatial accuracy rather than second order accuracy used in all other simulations. Flow visualizations and depth and width predictions revealed that quantitatively similar results can be expected from first order spatial settings. Although first order solutions will have less resolution than second order solutions, they may be beneficial in situations where stable second order solutions are challenging.

The next phase of Loci/GGFS validation assessment has already started. This next phase will cover several more PFGT-1 test runs and for longer simulated times. Tests typically ran for 10 seconds. Simulations will be executed much farther than the 1.0 second presented in this paper to see how Loci/GGFS fares in predicting long term cratering. Additional effort will be taken to match measured nozzle inlet conditions and actual *h*/*D* for each test. Effects of turbulence, mesh spacing near solid surfaces, and solver settings will also be explored.

References

[1] Gale, M., Buettner, K., Mehta, R., Liever, P. A., and Curtis, J., "Gas-Granular Flow Solver for Plume Surface Interaction and Cratering Simulations," AIAA Paper 2017-4503, *23rd AIAA Computational Fluid Dynamics Conference*, June 2017. doi: 10.2514/6.2017-4503

[2] Gale, M., Liever, P., Mehta, R., Yang J. and Curtis, J., "Realistic Regolith Models for Plume-Surface Interaction in Spacecraft Propulsive Landings," AIAA 2020-0797, *AIAA SCITECH 2020 Forum*, 2020. doi: 10.2514/6.2020-0797

[3] Luke, E., *A Rule-Based Specification System for Computational Fluid Dynamics*, PhD Dissertation, Mississippi State University, 1999.

[4] Weaver, A., Shurtz, T., Liever, P., Dawson, T., Howison, J., and West, J., "A Hybrid CFD/Engineering Model Tool for Lunar Lander Surface Erosion Prediction," *Earth and Space 2024: Engineering for Extreme Environments*, 2024.
doi: 10.1061/9780784485736.013

[5] Korzun, A. M., Eberhart, C. J., and West, J., "Overview of Plume-Surface Interaction Data from Subscale Inert Gas Testing at NASA MSFC Test Stand 300 Vacuum Facilities," AIAA 2022-1811. *AIAA SCITECH 2022 Forum*. January 2022.
doi: 10.2514/6.2022-1811

[6] Immer, C. M. and Metzger, P. T., "Rocket Cratering in Simulated Lunar and Martian Environments," *12th ASCE Earth & Space Conference*, Honolulu, HI, March 14-17, 2010.

[7] LaMarche, C. Q., Curtis, J. S., Metzger, P. T., "Permeability of JSC-1A: A lunar soil simulant," *Icarus*, Vol 212, No. 1, pp. 383-389, 2011.
doi: 10.1016/j.icarus.2010.12.015

[8] Metzger, P. T., Lane, J. E., Immer, C. D., Clements, S., "Cratering and blowing soil by rockets and engines during lunar landings," *Proceedings of the Sixth International Conference on Case Histories in Geotechnical Engineering*, Arlington, VA, August 11-16, 2008.

[9] Metzger, P. T., Immer, C. D., Donahue, C. M., Vu, B. T, Latta III, R. C., Deyo-Svendsen, M., "Jet-Induced Cratering of a Granular Surface with Application to Lunar Spaceports," *Journal of Aerospace Engineering*, Vol. 22, No. 1, pp. 24-32, 2009.
doi: 10.1061/(ASCE)0893-1321(2009)22:1(24)

[10] Guo, Y. and Curtis, J. S., "Discrete element method simulations for complex granular flows," *Annual Review of Fluid Mechanics*, Vol. 47, pp. 21-46, 2015.
doi: 10.1146/annurev-fluid-010814-014644

[11] Garzó, V., Dufty, J. W., & Hrenya, C. M., "Enskog theory for polydisperse granular mixtures. I Navier-Stokes order transport," *Phys. Rev. E*, Vol. 76, No. 3, 2007.
doi: 10.1103/PhysRevE.76.031303

[12] Garzó, V., Hrenya, C. M., & Dufty, J. W., "Enskog theory for polydisperse granular mixtures. II. Sonine polynomial approximation," *Phys. Rev. E*, Vol. 76, No. 3, 2007.
doi: 10.1103/PhysRevE.76.031304

[13] Murray, J. A., Benyahia, S., Metzger, P., and Hrenya, M., "Continuum representation of a continuous size distribution of particles engaged in rapid granular flow," *Physics of Fluids*, Vol. 24, 2012.
doi: 10.1063/1.4744987

[14] Murray, J. A., Garzó, V., & Hrenya, C. M., "Enskog theory for polydisperse granular mixtures III: Comparison of dense and dilute transport coefficients and equations of state for a binary mixture," *Powder Technology*, Vol. 220, pp. 24-36, 2012.
doi: 10.1016/j.powtec.2011.09.030

[15] Fontenot, R. L., Talbot, J., Gale, M., Mehta, R., "Modeling Enhancements for Eulerian-Eulerian Two-Fluid Methods in Compressible Particle-Laden Flows with Plume-Surface Interaction Applications," AIAA 2022-2195, *AIAA SCITECH 2022 Forum*, 2022.
doi: 10.2514/6.2022-2195

[16] Fontenot, R. L., Hunt, M., Harris, R., Gale, M., "Uncertainty Quantification in Crater Formation for Gas-Granular Flows due to Plume Surface Interaction," AIAA 2024-07866, *AIAA SCITECH 2024 Forum*, 2024.
doi: 10.2514/6.2024-0786

[17] van Wachem, B. G. M., Schouten, J. C., van den Bleek, C. M., Krishna, R., and Sinclair, J., "Comparative Analysis of CFD Models of Dense Gas-Solid Systems," *AIChE Journal*, Vol. 47, No. 5, May 2001.
doi: 10.1002/aic.690470510

[18] Guo, Y., Wassgren, C., Ketterhagen, W., Hancock, B., James, B., and Curtis, J., "A numerical study of granular shear flows of rod-like particles using the discrete element method," *Journal of Fluid Mechanics*, Vol. 713, 2012, pp. 1-26.
doi: 10.1017/jfm.2012.423

[19] Yang, J., Buettner, K. E., Guo, Y., Curtis, J. S., "Collisional dissipation rate for binary mixtures of aspherical particles," *Powder Technology*, Vol. 387, 2021, pp. 9-15.
doi: 10.1016/j.powtec.2021.03.056

[20] Liever, P. and West, J. S., "Particle Interaction Physics Model Formulation for Plume-Surface Interaction Erosion and Cratering," AIAA 2022-2317, *AIAA SCITECH 2022 Forum*, 2022.
doi: 10.2514/6.2022-2317

[21] Yang, J., Guo, Y., Buettner, K. E., and Curtis, J. S., "DEM investigation of shear flows of binary mixtures of non-spherical particles," *Chemical Engineering Science*, Vol. 202, pp. 383-391, 2022.
doi: 10.1016/j.ces.2019.03.027

[22] Howison, J., Gale, M., and Mehta, R., "An Automated Process to Generate Constitutive Models for Granular Mixtures Using LIGGGHTS," AIAA 2022-2194, *AIAA SCITECH 2022 Forum*, 2022.
doi: 10.2514/6.2022-2194

[23] Alshibli, K., Elnur, M., "Synchrotron Micro-Computed Tomography (SMT) Images of PB1 and JSC-1A Lunar Regolith Simulants," Dept. of Civil & Env. Engineering, University of Tennessee Knoxville, June 2022. Presentation to NASA Plume-Surface Interaction Project, Aug. 2022.

[24] Angelidakis, V., Nadimi, S., Otsubo, M. and Utili, S., "CLUMP: A Code Library to generate Universal Multi-sphere Particles." SoftwareX 15, p.100735, 2021.
[25] Gale, M., "Verification of the Eulerian-Eulerian Two-Fluid Model in Loci/GGFS," AIAA 2023-0283, *AIAA SCITECH 2023 Forum*, 2023.
doi: 10.2514/6.2023-0283
[26] West, J., Krolick, W., Liever, P., "Qualitative Comparison of Pathfinder Three-Dimensional Transient Gas Granular Simulation Results to Imagery from a Subscale, Reduced Pressure Plume Surface Interaction Ground Test," 13^{th} JANNAF Liquid Propulsion Meeting, Huntsville, AL, 2022.
[27] Korzun, A. M., Eberhart, C. J., West, J. S., Liever, P., Weaver, A. B., Mantovani, J. G., Langton, A. G., Kemmerer, B. W., Atkins, A. R., "Design of a Subscale, Inert Gas Test for Plume-Surface Interactions in a Reduced Pressure Environment," AIAA 2022-1808, *AIAA SCITECH 2022 Forum*, 2022.
doi: 10.2514/6.2022-1808